Instability and Transition due to Near-Critical Roughness in a Hypersonic Laminar Boundary Layer

Bradley M. Wheaton* and Steven P. Schneider†

School of Aeronautics and Astronautics, Purdue University, West Lafayette, IN 47907

Measurements of instability and transition were obtained in the wake of a cylindrical roughness within the laminar nozzle-wall boundary layer of the Purdue Mach-6 Quiet Tunnel. Using wall-mounted pressure transducers along the wake centerline, the root-mean-square pressure and power spectra were computed to find evidence of instabilities within the roughness wake. The roughness height was adjusted to explore the case of incipient transition on the nozzle wall. It appeared that small variations in the experimental parameters could have a large effect on transition for the near-critical case. Several dominant disturbance frequencies were identified for a range of conditions. These disturbances appear to be due to instabilities developing within the wake of the roughness. The streamwise evolution of these disturbances are reported, as well as the spanwise distribution at one streamwise location within the wake. These results can be used as a test case to continue to develop methods for computing the stability of roughness wakes.

Nomenclature

D	cylindrical roughness diameter, mm
k	cylindrical roughness height, mm
p_0	tunnel stagnation pressure, psia
p'	fluctuating component of pressure, psia
Re_∞	unit freestream Reynolds number, 1/m
Re_k	roughness Reynolds number, $\rho_k u_k k/\mu_k$
$\mathrm{Re}_{\mathrm{k,crit}}$	critical roughness Reynolds number
t	time after the diaphragm burst, s
T_0	tunnel stagnation temperature, K
T_{driver}	temperature from a thermocouple at the upstream end of the driver tube, K
$\overline{T}_{\mathrm{nozzle}}$	mean temperature recorded by the thermocouples on the nozzle, K
u	streamwise velocity, m/s
x	streamwise distance downstream from the central axis of the roughness, mm
z	spanwise arc length from the center of the roughness, mm

Greek

δ	boundary-layer thickness, defined as the height where the local velocity is 99.5% of the freestream value, mm
γ	ratio of specific heats
μ	dynamic viscosity, kg/m-s
ρ	density, kg/m^3

Subscripts

i	initial condition
k	roughness height condition
rms	root mean square
∞	freestream condition

Abbreviations

BAM6QT	Boeing/AFOSR Mach-6 Quiet Tunnel
RMS	Root Mean Square

*Research Assistant, Student Member AIAA. Present address: The Johns Hopkins University Applied Physics Laboratory, 11100 Johns Hopkins Rd., Laurel, MD, 20723.

†Professor, Associate Fellow AIAA

I. Introduction

A. Roughness-Induced Transition at Hypersonic Speeds

Boundary-layer transition is caused by disturbances that originate within the freestream or on the body, enter the boundary layer via receptivity mechanisms, grow through various instability modes, and cause turbulence.[1] Roughness on the surface of a reentry vehicle is among the many factors that can affect transition. Surface roughness can lead to boundary-layer transition at flight conditions where it is normally not present,[2] leading to increased heating that could exceed the design limits of a vehicle's thermal protection system. A roughness that does not alter transition is said to be subcritical. A critical roughness is a roughness of sufficient magnitude to induce transition upstream of the smooth-wall location. A roughness is said to be effective when transition moves as close to the roughness as is feasible.

For the case of a smooth wall, significant advances have been made in understanding the instability modes that cause transition. A greater understanding of these instabilities has led to the development of prediction methods that are based on the physics of transition. The e^N method[3–5] is an example of such a method and is used to predict smooth-wall transition. The e^N method has been extended to the hypersonic regime using the parabolized stability equations and used successfully to correlate transition.[6] Similar semi-empirical prediction methods are desired for roughness, but have yet to be developed.

Roughness-induced transition is currently estimated, out of necessity, using simple algebraic correlations based on empirical observations of transition. Wind tunnels, shock tunnels, and ballistic ranges are used to measure transition on subscale models that incorporate relevant forms of roughness. The measured transition location is then correlated to parameters such as $\mathrm{Re_k}$, the Reynolds number based on the roughness height k, and conditions in the undisturbed laminar boundary layer at the height k. Ideally, these test facilities should duplicate flight conditions such as Mach number, Reynolds number, enthalpy, surface temperature, ablation, freestream disturbance levels, and so on. However, for hypersonic flows it is not possible to design an experiment that includes all of these parametric effects, because no single test facility can simulate all aspects of hypersonic flight. Since these engineering correlations often use a data set that pertains to only a portion of the flight-relevant parameters, and the correlations include very little of the actual physics of the transition process, they can be subject to considerable uncertainty when used to predict transition in flight.

The mechanisms by which roughness affects transition are, at present, poorly understood. An isolated roughness element within a high-speed laminar boundary layer generates a wake region in which shock waves, separated flow, vortical structures, and unstable shear layers are often present.[7] The disturbed wake region can introduce an entirely new class of instability mechanisms that are not present in the smooth-wall boundary layer.[8–10] The degree to which the roughness element modifies the mean boundary-layer flow, and likely the corresponding dominant instability mechanism, depends on factors including the roughness height and shape, as well as the properties of the flow. However, there are very few quantitative measurements of these instabilities within the historical literature.

Thanks in large part to advancements in computational methods, researchers are recently beginning to characterize the mechanisms responsible for transition due to roughness at hypersonic speeds.[11–24] However, even direct numerical simulation must construct an appropriate grid and make assumptions regarding the input disturbance field when simulating these flows. In order to ensure that these computational methods are accurately simulating the physics of transition, controlled experimental measurements should be used to detect the real flow physics, select ideal test cases to be simulated, and confirm the findings of the computations. The end goal remains to develop effective prediction methods for roughness-induced transition that are feasible for use by the designers of flight vehicles.

B. Measuring Roughness-Induced Disturbances in the Boeing/AFOSR Mach-6 Quiet Tunnel

An isolated cylindrical roughness was used to introduce disturbances within the laminar nozzle-wall boundary layer of the Boeing/AFOSR Mach-6 Quiet Tunnel at Purdue University. Measurements were performed using flush-mounted fast pressure sensors within the roughness wake, to identify disturbances due to possible instability mechanisms. These measurements are the first such measurements at hypersonic speeds, and are meant to complement similar work at supersonic speeds[25,26] and low speeds.[27,28] Previous work by the authors[29,30] identified an instability due to a relatively large roughness that appeared to originate within the separation region upstream of the roughness, with the aid of direct numerical simulations by Bartkowicz et al.[15,22,31] at the University of Minnesota. Those results were for values of $\mathrm{Re_k}$ near 70,000. A roughness of

this magnitude is likely of interest to vehicle designers wishing to design effective trips that cause a boundary layer to transition. The present results pertain to transition due to smaller, near-critical roughness, with values of Re_k orders of magnitude lower than the previous results. These smaller roughness heights are of interest to vehicle designers who wish to predict the acceptable magnitude of roughness that will not cause transition in flight. These results should be part of a larger effort of measurements and computations that could be used in the development of physics-based transition prediction methods for isolated roughness elements in hypersonic flow.

II. Experimental Methods

A. Boeing/AFOSR Mach-6 Quiet Tunnel

The Boeing/AFOSR Mach-6 Quiet Tunnel (BAM6QT) at Purdue University is a low-noise hypersonic facility used mainly for transition research.[32,33] The BAM6QT uses a Ludwieg tube design (Figure 1). During operation, the tunnel is filled with high-pressure air while the region downstream of the diffuser is evacuated. Diaphragms are then broken to initiate the flow. An expansion wave then travels upstream into the driver tube. During the typical run time of several seconds, the pressure in the driver tube decreases quasi-statically and the freestream Reynolds number decreases. The Reynolds number is constant for 0.2-s increments as the expansion wave reflects within the driver tube.

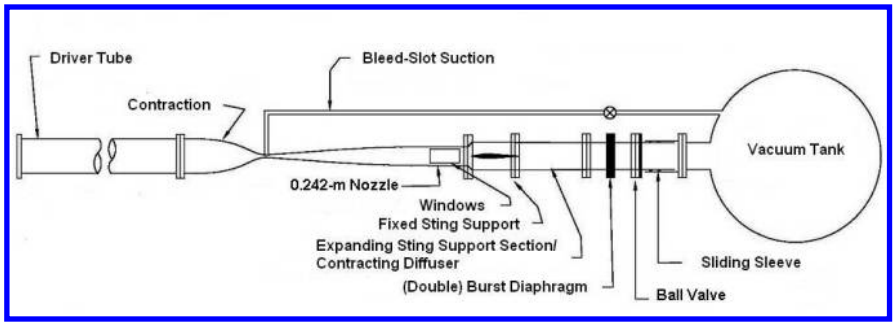

Figure 1. Schematic of the Boeing/AFOSR Mach-6 Quiet Tunnel.

A laminar boundary layer on the nozzle wall of the BAM6QT enables low-noise operation, and also made it possible to measure instabilities induced by a roughness element. Several design features permit the tunnel to be operated with a laminar boundary layer on the nozzle wall.[33] At the conditions in these experiments, this laminar nozzle-wall boundary layer is on the order of 8 mm thick, an order of magnitude thicker than typical hypersonic boundary layers on a wind-tunnel model. In this work, a cylindrical roughness was placed on the nozzle wall within a laminar boundary layer and used to introduce disturbances. The unusually thick boundary layer was advantageous to increase the spatial resolution of the measurements, reduce the effects of probe interference, and reduce the instability frequencies, so that a larger range of instrumentation could be used to detect these frequencies. The end of the nozzle serves as the test section of the BAM6QT. Contoured inserts are used in these experiments for optical access, placement of instrumentation, and placement of the roughness element.

B. Cylindrical Roughness Element

A 5.97-mm-diameter Starrett model 263L-38TN micrometer head was used as a convenient cylindrical roughness element in these experiments (Figure 2). A cylindrical roughness element was initially chosen because of its elementary shape, easily adjustable height, and the wide availability of cylindrical-shaped micrometers. Between runs, the height k of the micrometer can be adjusted from 0.00-24.31 mm with a precision of ± 0.05 mm. The roughness element was located in the nozzle of the Boeing/AFOSR Mach-6 Quiet Tunnel at an axial location of 1.924 m from the throat. A coordinate system is used here with an origin at the center of the roughness at the wall. The coordinate x is the axial (streamwise) distance downstream of the roughness. Note that x is not the arc length along the nozzle surface. The coordinate z is the spanwise arc length from the roughness centerline along the curved nozzle interior. The coordinates were nondimensionalized by the roughness diameter, D.

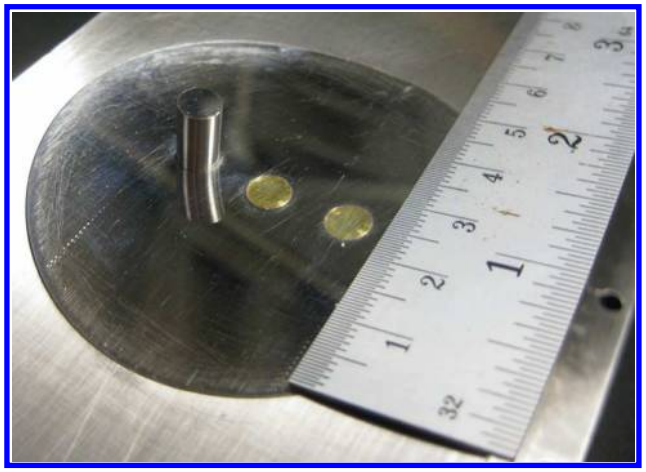

Figure 2. Variable-height cylindrical roughness element with 5.97-mm diameter. A scale with centimeters and inches is shown for reference.

C. Kulite XCQ-062-15A Pressure Transducers

Kulite XCQ-062-15A pressure transducers were mounted flush to the nozzle wall along the centerline of the roughness wake. The Kulite XCQ-062-15A consists of a strain gauge on a 1.68-mm-diameter silicon diaphragm. The sensor has a range of 0–15 psia and a resonance frequency typically between 200–300 kHz. A mechanical stop at pressures greater than 15 psia protects the sensor from damage as the tunnel is filled to the desired stagnation pressure prior to a run. The manufacturer's "A-screen" was used for these sensors, as opposed to the more protective "B-screen". The A-screen has a large central cavity that offers limited protection of the sensor diaphragm, but with an improved dynamic response that is flat to 30–40% of the resonance frequency.

The A-screen sensors have a cavity exposing the sensor to the flow. This cavity has a depth of 1.02 mm, which is approximately 13% of the boundary-layer thickness at a stagnation pressure of 90 psia. The cavity was assumed to have minimal interference with the flow. The diameter of the cavity is also 1.02 mm. A MATLAB code was written to verify that the transducer was sufficiently small to eliminate attenuation for the frequencies measured in this work. The sensor face was modeled as a circle using 400 grid points. Because the spatial distribution of the disturbances in the roughness wake were unknown, the disturbances were modeled as two-dimensional traveling sine waves with a convection velocity equal to the freestream velocity. For one wave cycle, the root-mean-square amplitude of the disturbance was calculated from an average value across the sensor face, and compared to the theoretical root-mean-square amplitude of a sine wave. The results showed minimal attenuation for the frequencies measured in this paper. For disturbances at 120 kHz, attenuation was merely two percent. An attenuation of 3 dB occurred at a frequency of 750 kHz, well above the measurement range of the sensor.

D. Apparatus for Pressure-Sensor Measurements

The sensors were mounted with either Loctite 222MS (or 2440) thread-locking adhesive, or cosmetic nail polish. Custom electronics were used to provide a 10-V excitation signal for the transducer, and to process the voltage output of the transducer. The transducer output was amplified with a gain of 100 using a INA103 amplifier chip to give a DC voltage output. This DC voltage varies linearly with pressure. Static calibrations of each sensor were performed in-situ, using the vacuum that normally occurs after a run. A new calibration was taken during each tunnel entry. A Paroscientific Model 740 Standard quartz pressure transducer was used for the calibrations, with a full-scale reading of 30 psia and an accuracy of better than 0.008% of full scale.

Figure 3 shows photographs of the apparatus, taken from the end of the nozzle. A view looking upstream from the end of the nozzle is shown in Figure 3(a). The roughness and pressure sensors were placed on the upper wall of the nozzle. Pressure sensors were placed within the slot normally used for probe insertion. The left hand side of the image shows the nozzle wall hot-film array. The signals from two wall hot films were monitored during each run to ensure that the nozzle-wall boundary layer remained laminar and attached.

Because the hot-film array was offset 90° azimuthally from the roughness, the wake of the roughness was not expected to interfere with the boundary layer there. The right hand side of the image shows the large plexiglass window. In Figure 3(a), the roughness was placed off the centerplane of the nozzle. However, for these experiments the roughness was located on the centerplane of the nozzle, such that the pressure sensors were measuring along the centerline of the roughness wake.

A cylindrical insert was placed downstream of the nozzle exit, and used to continue the nozzle flow into the diffuser section. This "multi-ring pipe insert" contained a series of interchangeable rings in which additional pressure sensors were placed (Figure 3(b)). The multi-ring pipe insert extends the measurement range of the apparatus from $x/D = 93.1$ to $x/D = 152.0$. Experiments by Casper[34] have verified that the laminar boundary layer extends beyond the nozzle exit along the pipe insert, however with a greater likelihood of intermittent disturbances when near the maximum stagnation pressures required for quiet flow. The results in this work are at significantly lower Reynolds numbers and intermittent disturbances were seldom observed. Sensors were placed at $x/D = 46.3$, 63.3, 76.1, 93.1, 118.0, 126.5, 135.0, 143.5, and 152.0. An array of spanwise sensors was placed within the multi-ring pipe insert at $x/D = 143.5$, as seen in Figure 3(b). This spanwise array contained sensors at $z/D = 0.0$, 1.8, 3.5, $\pm$5.3, 7.1, and $\pm$10.6.

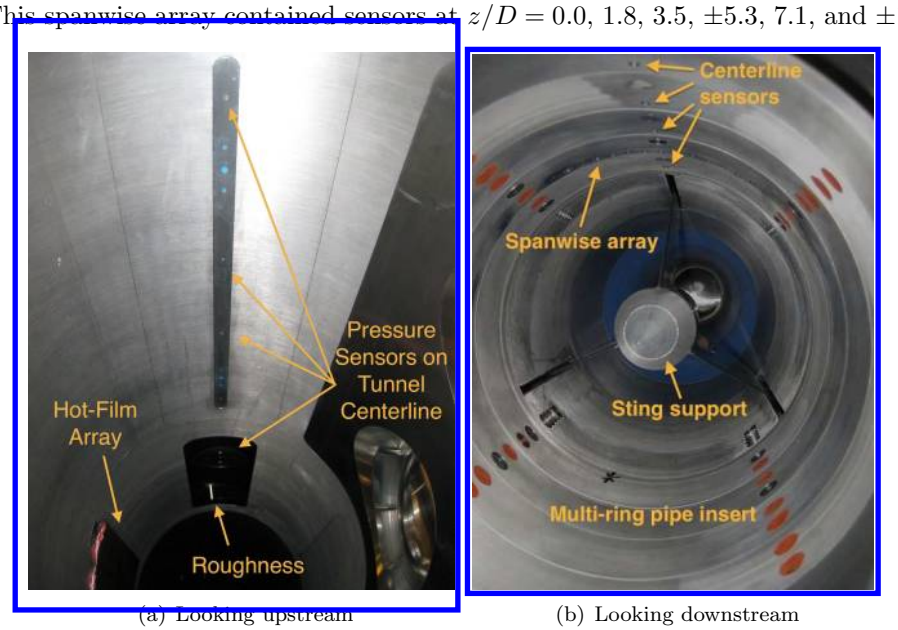

(a) Looking upstream (b) Looking downstream

Figure 3. Apparatus for non-intrusive surface-pressure measurements. Photographs taken from the end of the nozzle.

E. Data Acquisition and Processing

Data were sampled at 500 kHz in Hi-Res mode on Tektronix oscilloscopes. Hi-Res mode is a method of digital filtering in which the scope acquires data at its maximum sampling frequency of 500 MHz. The data are then averaged in real time to produce the desired sampling frequency. For example, when a sampling frequency of 500 kHz is desired the scope computes a real-time average over 1,000-point intervals to record an averaged result at 500 kHz. This mode effectively acts as a low-pass filter to eliminate signal aliasing, with 3 dB of attenuation at 0.44 times the sampling frequency. When using Hi-Res mode, the analog electronics in the oscilloscope are supposed to be sufficiently linear to increase the effective bits of resolution from 8 to approximately 12.

For post-processing, the data were separated into 0.05-s samples. Pressure measurements on the wall were nondimensionalized by the static pressure (p_∞). Power spectral densities were calculated from the samples using Blackman windows with 50% overlap. The window size was 1/40th of the 0.05-s sample for a total of 625 points, resulting in a total of 80 windows. The frequency resolution of the spectra using these methods was 0.5 kHz. In the spectra plots, only every fourth point is plotted for clarity. The RMS of frequency bands of interest was calculated by numerically integrating the area under the power spectrum. The integration resulted in the power of the frequency band in Pa^2 or $(N/m^2)^2$. The square root of that number gave the

RMS of the frequency band. The RMS was calculated over the frequency range of 0–100 kHz to avoid the effect of sensor resonance at higher frequencies. When time traces were plotted, the data were digitally low-pass filtered at 150 kHz using an 8-pole Butterworth filter to remove any effects of sensor resonance. All data appearing in the spectra were unfiltered.

F. Calculation of Reynolds Numbers

The initial and instantaneous stagnation pressures were used to compute the freestream Reynolds number and the instantaneous stagnation temperature. The initial stagnation temperature was assumed to be 433 K, as this is the set point for the driver tube heaters. While the initial stagnation temperature likely has small variations between runs, there is no method to measure an accurate temperature across the entire driver tube. During the run, the stagnation temperature decreases along with the stagnation pressure. Because there is presently no method to measure the instantaneous stagnation temperature, it was estimated using the isentropic relation

$$T_0 = T_{0,i} \left(\frac{p_0}{p_{0,i}} \right)^{\frac{\gamma-1}{\gamma}} \tag{1}$$

where p_0 and T_0 are the instantaneous stagnation pressure and temperature, and $p_{0,i}$ and $T_{0,i}$ are the initial values at the start of the run. The perfect gas law was used to calculate the freestream density (ρ_∞) and Sutherland's law was used for the dynamic viscosity (μ_∞). An alternative method for estimating the stagnation temperature is presented in Estorf et al.[35]

The roughness Reynolds number ($\mathrm{Re_k}$, or $\rho_k u_k k/\mu_k$) was calculated using results from the Harris[36] finite-difference boundary-layer code. The best estimate for the equilibrium temperature distribution on the interior of the nozzle was obtained from Skoch[37,38] using a finite element heat transfer simulation (see Section III). The simulation predicted the temperature for the initial 0.88 m of the nozzle, and the remainder of the nozzle was assumed to be 298 K.

III. Characterization of the Smooth-Wall Boundary Layer

A. Calculation of Boundary-Layer Profiles using the Harris Code

In order to calculate flow properties such as the roughness Reynolds number ($\mathrm{Re_k}$) or the boundary-layer thickness (δ), a simulation of the incoming laminar boundary layer was performed. The Sivells[39] method of characteristics code and the Harris[36] finite difference boundary layer code were used to compute the laminar nozzle-wall boundary layer. However, the Harris code requires a temperature distribution along the interior of the nozzle in order to compute the boundary layer. An accurate nozzle temperature distribution was also desired for any computations of the roughness wake performed by others.

B. Measurements of the Nozzle-Wall Temperatures

There are presently no means to obtain experimental measurements of the entire temperature distribution along the interior surface of the nozzle. Permanent installation of thermocouples on the interior surface of the nozzle would disturb the laminar boundary layer necessary to obtain quiet flow. Even temporary installation of thermocouples could cause damage to the smooth interior surface of the nozzle. An assumed temperature distribution must be generated using a combination of thermocouple measurements of the temperature on the exterior of the nozzle as well as finite-element heat transfer analyses using estimates for the temperature boundary conditions.

Thirty-six type J thermocouples were installed on the exterior of the nozzle by Steen[40] in 2010. The thermocouples were attached with thermal paste and held in place using band clamps. No insulation was present over the thermocouples. The thermocouples were mounted at 90° azimuthal increments along the exterior of the nozzle within a range of axial locations of 0.17–1.71 m from the throat. The majority of the thermocouples were installed along the north side of the nozzle, with additional thermocouples on the south side as well as the top and bottom walls. Thermocouple measurements along the exterior of the nozzle were obtained in order to compare to estimations of the temperature distribution of the nozzle.

The nozzle temperature has been observed to increase during a typical day of testing.[40] This heating likely occurs as high-temperature air from the driver tube is blown into the vacuum tank after the hypersonic portion of the run has ended. Thermocouple measurements of the temperature of the nozzle were recorded

to determine the magnitude of the temperature increase. Harris code calculations were then performed using different temperature profiles to determine the effect of temperature on the boundary-layer properties at the location of the roughness.

C. Effect of Temperature on Computed Boundary-Layer Properties

The best estimate for the equilibrium temperature distribution on the interior of the nozzle was obtained by Skoch[37,38] using a Finite Element Heat Transfer (FEHT) simulation for heat transfer in the nozzle. In the simulation, Skoch modeled the initial 0.88 m of the nozzle. Several boundary conditions were tested, but the results discussed here used a 433 K and 298 K isothermal boundary condition on the upstream and downstream edges of the simulation, respectively. The interior surface of the nozzle was set to adiabatic, since the simulation was for equilibrium conditions. The exterior surface of the nozzle was modeled using convective heat transfer. Note that the simulation assumed axisymmetric heat transfer, however as shown earlier, the top wall of the nozzle is often warmer than the other walls. The temperature distribution for the interior of the nozzle, from the FEHT, was one of the temperature distributions used in the Harris code to estimate the nozzle-wall boundary layer properties. The Skoch FEHT analysis only modeled the initial 0.88 m of the nozzle, because regions downstream of this location were at room temperature. Thus, in the Harris code, the portion of the nozzle downstream of 0.88 m was set to a constant temperature of 298 K. This temperature distribution will be referred to as the "FEHT 298 K" profile to denote the temperature assumption for the downstream portion of the nozzle.

Several temperature distributions were used to compute the effect of increased nozzle temperatures on the boundary layer properties at the roughness location (Figure 4). Calculations were performed using three different nozzle-wall temperature distributions: the Skoch FEHT 298 K distribution, the FEHT analysis scaled to 308 K instead of 298 K, and an isothermal 300 K profile similar to that used in the Minnesota computations.[15,22] The solid blue line shows the Skoch FEHT 298 K results for the interior of the nozzle. The FEHT 298 K results for the exterior of the nozzle are shown as the dashed green line. To simulate the effects of an increase in nozzle temperature, the FEHT results for the interior of the nozzle were scaled using a linearly increasing factor to create a 308 K boundary condition at the downstream end of the nozzle. The scaled distribution is the dashed red line in the figure, and additional Harris code results were generated using this temperature assumption. The isothermal 300 K assumption is shown as the dashed black line. Note that the isothermal assumption is likely to underpredict the temperatures for the initial 0.5 m of the nozzle. Also shown in Figure 4 are the maximum and minimum temperatures from a single tunnel entry of 55 runs. Note again that these measured temperatures are from thermocouples on the exterior of the nozzle, while the computed temperature distributions are from the interior of the nozzle. However, the FEHT 298 K prediction for the exterior nozzle temperatures is similar to the predictions for the interior nozzle temperatures. The measurements show that the FEHT 298 K and 308 K profiles are decent approximations for the nozzle temperature extremes seen during normal operation of the tunnel.

The nozzle temperature assumption thus has an effect on the estimation of the roughness Reynolds number, $\mathrm{Re_k}$. A hotter wall temperature will decrease $\mathrm{Re_k}$. In this case, $\mathrm{Re_k}$ is defined as $\rho_k u_k k/\mu_k$, where the subscript k denotes the conditions in the undisturbed laminar boundary layer at the roughness height k. Other definitions may use the values of these properties at the wall or at the boundary-layer edge. Figure 5(a) shows the value of $\mathrm{Re_k}$ versus roughness height. The same data are also presented in Figure 5(b) with a log scale for the vertical axis. There is a large variation of $\mathrm{Re_k}$ with roughness height due to several factors. As the roughness height is increased, the local mass flux also increases while the dynamic viscosity decreases by nearly an order of magnitude.

All values of $\mathrm{Re_k}$ reported in this work use the FEHT 298 K results, as this is the best estimate for the nominal distribution of the temperature on the interior of the nozzle. Figure 5(c) shows the percent difference in the calculated values of $\mathrm{Re_k}$ if either the FEHT 308 K or the isothermal 300 K temperature distributions were used. Again, the FEHT 308 K distribution is an estimate for the maximum observed nozzle temperature extreme. The isothermal 300 K profile is a simplification that could be made in simulations of this work, if it would be nontrivial to include a complex temperature distribution in the simulations. The percent difference is not computed at $k = 0$ mm, since $\mathrm{Re_k}$ is zero at the wall, and there is a singularity in the computed percent difference at the wall. The percent difference is calculated at heights of 0.001 mm and greater. However, there is potential for numerical rounding errors near the wall due to small values of $\mathrm{Re_k}$.

In general, the FEHT 308 K assumption decreases $\mathrm{Re_k}$ by approximately 7% for the smaller roughness heights of 0–4 mm (for example, the results shown in this paper). The largest changes in $\mathrm{Re_k}$ occur for

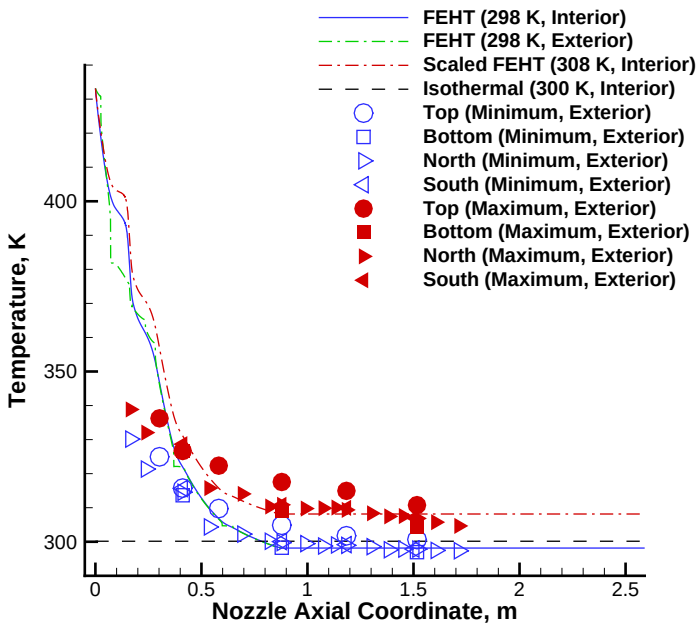

Figure 4. Nozzle temperature distributions used for the Harris code calculations. Observed maximum and minimum temperatures on the external surface of the nozzle during a single tunnel entry are also shown.

roughness heights of 4–9 mm, where $\mathrm{Re_k}$ decreases by 10–13%. Above $k = 9$ mm, the calculated value of $\mathrm{Re_k}$ does not change because these heights are outside of the boundary layer, in the freestream flow. The isothermal 300 K assumption increases the computed values of $\mathrm{Re_k}$ for roughness heights of 4–9 mm.

IV. Effect of Roughness Height on Incipient Transition on the Nozzle Wall

A. Nominal Test Conditions

Experiments were performed at a nominally similar Reynolds number to identify the roughness height at which incipient transition occurred at the downstream end of the experimental apparatus (up to $x/D = 152.0$). Several roughness heights were tested at the nominal condition appearing in Table 1. The runs were performed at a nominal initial stagnation pressure ($p_{0,i}$) of 95 psia. The initial stagnation pressure was always within one percent of this nominal value. Data were analyzed at a time (t) of 1.00–1.05 s after the diaphragms were burst, resulting in a nominal stagnation pressure of 89 psia. Note that additional results from $t = 1.50$–1.55 s and $t = 2.00$–2.05 s will be shown later. The estimated first- and second-mode frequencies at the condition in Table 1 are 11.3 kHz and 56.6 kHz, respectively. These frequencies were estimated from the Harris code results, using $u_e/2\delta$ for the second-mode instability and $u_e/10\delta$ for the first-mode instability.

B. Effect of Roughness Height on RMS Pressure

The RMS pressures from several sensors on the roughness wake centerline and downstream of the roughness are plotted in Figure 6. The RMS pressure was calculated by numerically integrating the power spectrum from 0 to 100 kHz as discussed in Section II, and is nondimensionalized by the static pressure (p_∞). Each sensor location is denoted by a symbol and the horizontal axis is the streamwise coordinate x/D. Typical smooth-wall laminar and turbulent levels are also plotted.

The boundary layer on the nozzle wall remains laminar for roughness heights of 2.54 mm and below, as indicated by RMS pressures near the smooth-wall laminar levels. However, for a roughness height only slightly larger (2.79 mm), evidence of transition is seen at the downstream end of the measurement range. The RMS begins to depart from smooth-wall laminar levels near $x/D = 120$ and increases sharply downstream,

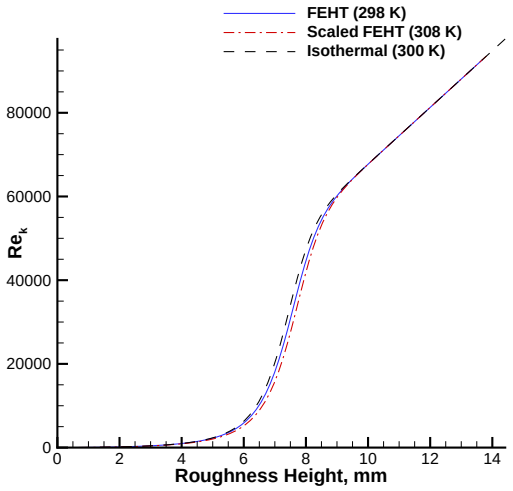

(a) Linear Scale

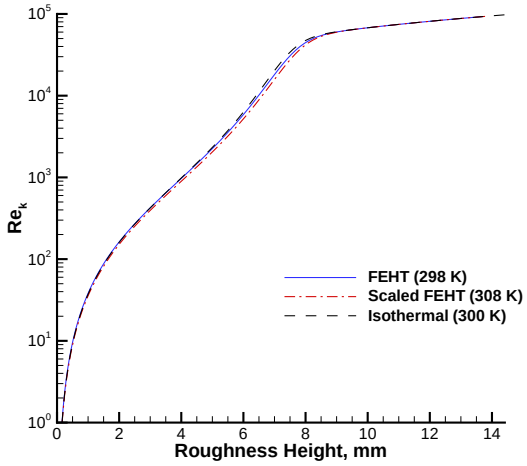

(b) Semilog Scale

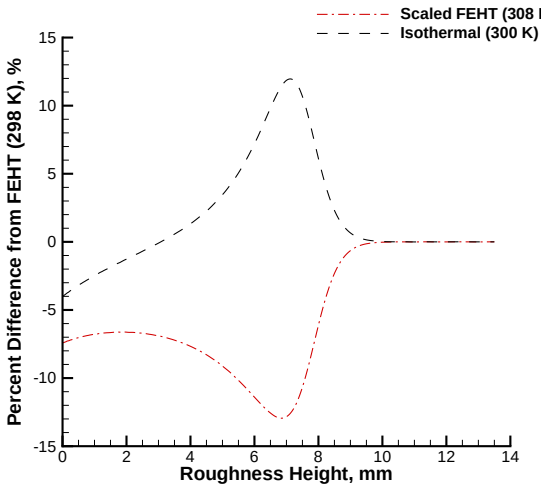

(c) Percent Difference from FEHT 298 K

Figure 5. Computed $\mathrm{Re_k}$ vs. roughness height for several nozzle temperature distributions (nozzle axial location of 1.924 m and $p_0 = 90$ psia).

Table 1. Nominal condition for data appearing in this paper, unless otherwise indicated.

Initial stagnation pressure	$p_{0,i}$	95 psia
Initial stagnation temperature	$T_{0,i}$	433 K
Time during run	t	1.00–1.05 s
Stagnation pressure	p_0	89 psia
Stagnation temperature	T_0	425 K
Unit Reynolds number	Re_∞	6.88×10^6/m
Boundary-layer thickness	δ	7.7 mm

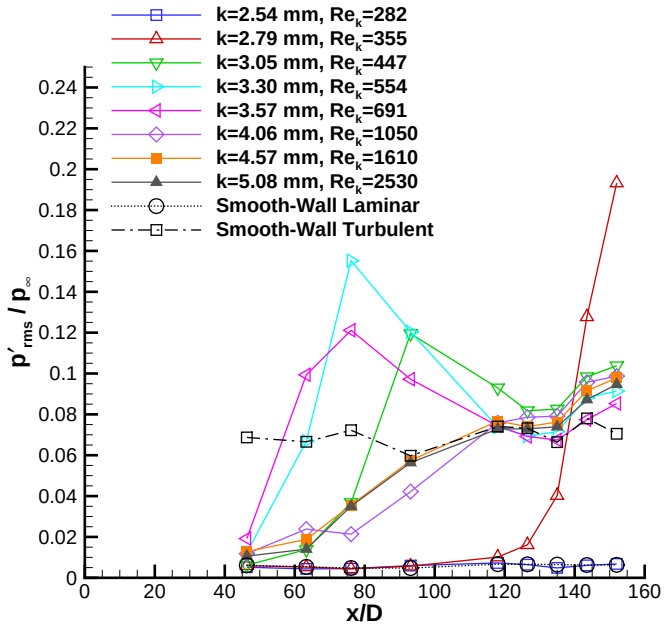

Figure 6. Root-mean-square pressure fluctuations downstream of several roughness heights.

increasing to a level of over twice the smooth-wall turbulent value. For roughness heights of 3.05, 3.30, and 3.57 mm, there is a peak in the RMS. The RMS overshoots the smooth-wall turbulent value and then decreases farther downstream. This overshoot is typical, as maximum RMS pressures are often observed within transitional flow.[41] The peak in the RMS moves forward with increasing k as expected. This trend indicates that transition occurs, as the RMS eventually recovers to values near those of a turbulent boundary layer. For the largest group of roughness heights (4.06, 4.57, and 5.08 mm), the RMS values appear fairly similar. As the height of the roughness increases, the spanwise extent of the wake is expected to increase. It is possible that the wake will eventually widen to the extent that most of the disturbances leading to transition occur somewhere off the wake centerline. The centerline RMS values for heights of 4.06, 4.57, and 5.08 mm are lower than for heights of 3.05, 3.30, and 3.57 mm, possibly due to variations in the spanwise extent of the wake.

It would appear that a roughness height of 2.79 mm is the height at which incipient transition occurs at the downstream end of the apparatus, for this experimental condition and configuration. Thus, roughness heights near 2.79 mm are referred to here as "near critical". A roughness height of 2.79 mm corresponds to $\mathrm{Re_k} = 355$, which is assumed to be the approximate value of $\mathrm{Re_{k,crit}}$ for this case. In this case, a truly "critical" roughness cannot be defined, as the natural smooth-wall transition location was not observed within the measurement range of the apparatus. This paper makes the assumption that the observed value of near-critical roughness is approximately equal to the actual value of critical roughness, $\mathrm{Re_{k,crit}}$.

As a result of a lack of historical data for isolated roughness at Mach 6, it is difficult to place the present observed value of $\mathrm{Re_{k,crit}} = 355$ into historical context. A good summary of low-speed observations of $\mathrm{Re_{k,crit}}$ appears in Smith and Clutter,[42] who estimated that roughness at low speeds with $\mathrm{Re_k} \leq 25$ would not cause transition. However, historical observations of $\mathrm{Re_{k,crit}}$ at supersonic and hypersonic speeds are limited. It is difficult to perform an experiment to measure critical roughness, since a baseline smooth-wall transition location must first be established and incremental roughness heights must be tested to observe the deviation of transition from the smooth-wall case. Historical observations of $\mathrm{Re_{k,crit}}$ in the literature vary greatly due to inconsistencies in the author's definition of critical roughness, the author's definition of $\mathrm{Re_k}$, and a lack of data with a consistent set of experimental conditions. These conditions include roughness shape, freestream Mach number, and wind tunnel test geometry, all of which could affect $\mathrm{Re_{k,crit}}$. For example, Van Driest et al.[43,44] calculate $\mathrm{Re_k}$ using the boundary-layer edge conditions instead of the local conditions. Smith and Clutter[42] show observations of critical roughness at supersonic speeds, but for two-dimensional

roughness, using conditions behind a normal shock to calculate Re_k. Holloway and Sterrett[45] appear to show critical roughness data for isolated roughness at Mach 6, however their definition of "critical" roughness is more similar to the present definition of "effective" roughness. Reda[46] uses the wall viscosity instead of the local viscosity to compute Re_k, and estimates a critical roughness Reynolds number of approximately 800–1000, for isolated roughness on a hemispherical geometry at a freestream Mach number of 12. Reda does not observe transition for the smooth-wall case in these experiments and his edge Mach numbers are significantly lower than in the present work. Casper et al.[47] observed the onset of transition for Re_k of approximately 100–200, on a 7° half-angle cone under quiet flow at Mach 6. Casper's numbers are generally similar to the present values.

C. Time Traces of Surface Pressure along the Wake Centerline

Figure 7 shows time traces of the surface pressure signal from $t = 1.000$ s to $t = 1.005$ s for roughness heights of 2.79, 3.05, and 3.30 mm. The time traces are from the same data that appear in Figure 6. The traces have been low-pass filtered to attenuate effects of high-frequency sensor resonance as described in Section II. The left vertical axis shows the fluctuating component of the pressure signal (p') nondimensionalized by the freestream pressure (p_∞). Each trace has been offset vertically to correspond to the distance downstream from the roughness x/D. The right vertical axis indicates the distance downstream from the roughness.

In Figure 7(a), the pressure time traces are shown for the roughness height of 2.79 mm. Prior to $x/D = 118.0$, the boundary layer RMS pressure remains at laminar levels. At $x/D = 118.0$ and $x/D = 126.5$, small oscillations can be seen in the pressure signal. These oscillations grow in amplitude downstream. At $x/D = 135.0$ and $t = 1.0045$ s, a potential wave packet can be seen with an amplitude significantly higher than the rest of the oscillations. The occurrence of these bursts and the increasingly random oscillations farther downstream are consistent with breakdown to turbulent flow. The RMS pressure does indicate that transition may be occurring at the downstream end of the apparatus for this roughness height.

As the roughness height is increased to 3.05 mm (Figure 7(b)), the location at which the oscillations are first visible in the pressure traces moves farther upstream because transition moves forward. Small oscillations can be seen at $x/D = 63.3$ and begin to occur in packet-like "bursts" at $x/D = 76.1$. The traces are random and chaotic by $x/D = 118.0$ and beyond. For $k = 3.30$ mm (Figure 7(c)), the oscillations are first seen farther upstream at $x/D = 46.3$, indicating that transition is moving forward again as expected.

D. Repeatability of Transition for Small Roughness Heights

For certain roughness heights, repeated runs suggested that small variations in the experimental parameters could have an effect on the transition location, and thus the repeatability of these cases. Several repeated runs were performed for smaller roughness heights that cause incipient transition on the nozzle wall. The effect of the experimental parameters on the repeatability of these cases will be explained in this section. The effect of small changes in experimental conditions on transition is consistent with historical data showing that for critical roughness, the transition location moves quickly forward for small changes in conditions.[43,44]

For each run, the initial stagnation pressures were matched as closely as possible to replicate similar flow conditions. However, it is difficult to replicate the exact stagnation pressure for repeated runs. Variations in nozzle heating are also likely to have an effect on the repeatability of these small roughness heights, as described in Section III. For example, over the course of fifty similar runs during a single tunnel entry, the initial stagnation pressure varied from 94.8 psia to 95.9 psia with an average of 95.2 psia. Table 2 shows the mean, maximum, and minimum conditions for these runs. The table shows the initial stagnation pressure, the temperature of the thermocouple at the upstream end of the driver tube recorded immediately prior to the run (T_{driver}), and the average of all thermocouples on the exterior of the nozzle wall recorded immediately prior to the run ($\overline{T}_{\mathrm{nozzle}}$). The nominal driver tube air temperature should be 433 K. While the thermocouple measuring T_{driver} only provides the temperature at the far upstream end of the driver tube, it may be an indication of variations in driver tube air temperature between runs. The absolute variation of these properties during all the runs was less than two percent, but nevertheless the variation could have been large enough to cause differences in the results for small, near-critical roughness heights.

Data from repeated runs similar to those in Figure 6 were gathered and the results appear in Figure 8. Roughness heights of 2.79, 3.05, and 3.30 mm are plotted. The line color corresponds to repeated runs for a particular range of roughness heights, and each letter symbol corresponds to a particular run. Additional data for heights of 2.27, 2.54, and 2.67 mm were available, but were not plotted since the boundary layer

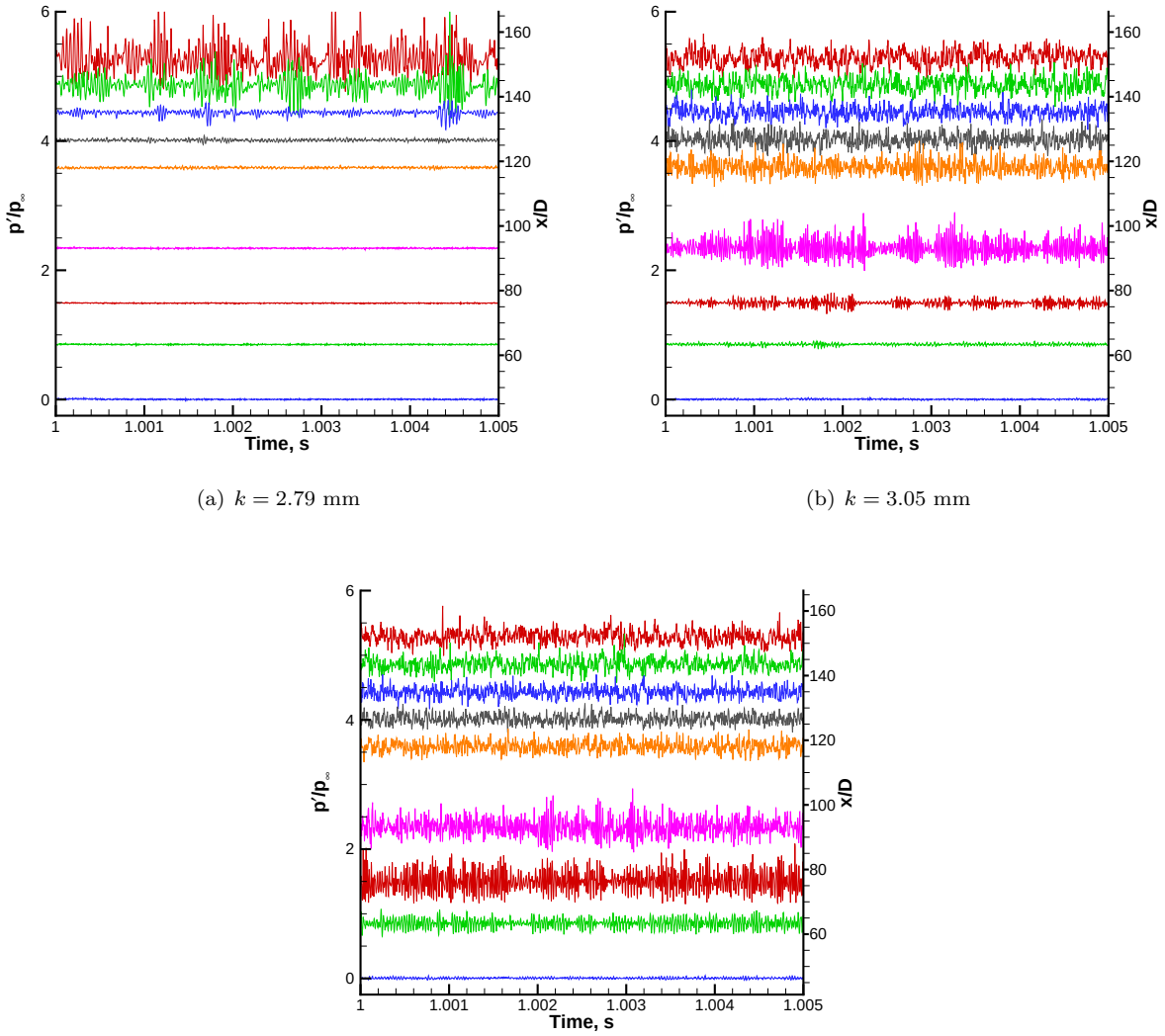

(a) $k = 2.79$ mm

(b) $k = 3.05$ mm

(c) $k = 3.30$ mm

Figure 7. Pressure traces for $p_{0,i} = 95$ psia and $t = 1.0$ s

Table 2. Variation of run conditions for fifty nominally-similar runs.

	Mean	Maximum	Minimum	Maximum Diff. (%)	Minimum Diff. (%)
$p_{0,i}$ (psia)	95.2	95.9	94.8	+0.7	−0.4
T_{driver} (K)	431.0	437.0	426.5	+1.4	−1.0
$\overline{T}_{\text{nozzle}}$ (K)	310.5	315.0	304.6	+1.4	−1.9

remained laminar for these heights. The runs are from several different tunnel entries, at random times during the day, to account for variations in nozzle heating. The largest roughness heights of 3.05 and 3.30 mm are fairly repeatable, with some scatter in the calculated RMS pressure. The RMS pressure due to the intermediate roughness height of 2.79 mm, however, varies during repeated runs. For some runs, the RMS values are similar to those for a laminar boundary layer. For others, transition onset appears to occur. The variation in the RMS pressure appears to be largest for this near-critical height. This variation is thought to be due to the critical nature of roughness-induced transition. It is likely that this particular roughness height, at these particular conditions, is highly sensitive to variations in the experimental parameters.

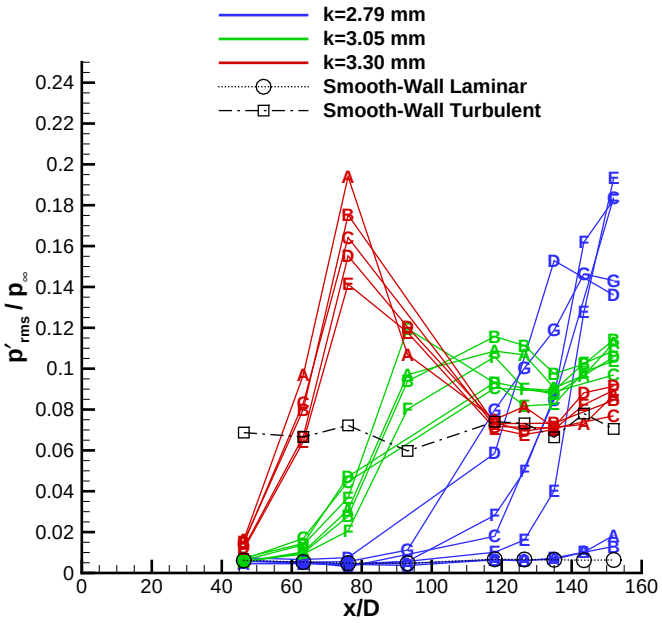

Figure 8. Repeatability of RMS pressure fluctuations downstream of several roughness heights.

V. Effect of Incremental Changes in Roughness Reynolds Number

Previous results in this paper have indicated that incipient instability and transition in the wake of the roughness element is highly sensitive to small changes in the roughness height for a constant Reynolds number. This section will explore the effect of incremental changes in the roughness Reynolds number $\mathrm{Re_k}$ on the RMS pressure and spectra downstream of the roughness. The manner in which the BAM6QT operates was advantageous for this study. Because the tunnel Reynolds number decreases quasi-statically during a single run, the effect of small changes in freestream conditions can be examined by analyzing data from different times during the run. Previously in this section, most data have been analyzed for runs with an initial stagnation pressure $p_{0,i} = 95$ psia at $t = 1.00$–1.05 s into the run. This time was chosen because the transient tunnel startup process ends approximately 0.7 s the diaphragms are broken at $t = 0.0$ s.

Previous results have been shown for roughness heights of 2.79, 3.05, and 3.30 mm at $t = 1.0$ s. This section will show additional results for these heights at $t = 1.50$–1.55 s and $t = 2.00$–2.05 s. Results at times much greater than $t = 2.05$ s cannot be used due to increased levels of tunnel noise that occur near the end of the run.[48] The analysis of different times during each run results in data at a variety of values of $\mathrm{Re_k}$ from approximately 300–550, and the effect of small changes in $\mathrm{Re_k}$ within this region can be examined. Table 3 shows the precise conditions for the data shown in this section, from three different runs. As described earlier, the calculation of $\mathrm{Re_k}$ is an estimate based on the FEHT 298 K temperature distribution of the nozzle, and for these conditions could decrease by as much as 7% for a 10 K increase in nozzle temperature. The conditions are listed with $\mathrm{Re_k}$ in ascending order. Data analyzed at the end of each run will have a lower value of $\mathrm{Re_k}$ because the roughness height is constant and the boundary layer is thicker. Since results from multiple heights are shown together here, it should be noted that changing the roughness height changes the

roughness shape ratio k/D, since the diameter of the roughness is fixed. The effect of k/D on the instability mechanisms is unknown, but the change in k/D is small enough here that the effect is presumed to be small.

Table 3. Conditions for examining the effect of $\mathrm{Re_k}$ on incipient instability and transition.

k (mm)	k/D	t (s)	$p_{0,i}$ (psia)	p_0 (psia)	T_0 (K)	$\mathrm{Re_k}$ (FEHT 298 K)
2.79	0.47	2.0	94.9	82.4	415.9	322
2.79	0.47	1.5	94.9	85.6	420.4	339
2.79	0.47	1.0	94.9	88.6	424.6	355
3.05	0.51	2.0	95.1	82.7	416.0	404
3.05	0.51	1.5	95.1	85.8	420.5	426
3.05	0.51	1.0	95.1	88.9	424.7	447
3.30	0.55	2.0	94.9	82.5	416.0	499
3.30	0.55	1.5	94.9	85.6	420.4	526
3.30	0.55	1.0	94.9	88.7	424.7	554

A. Streamwise and Spanwise RMS Pressure

Figure 9(a) shows the RMS pressure along the centerline of the wake of the roughness for the conditions listed in Table 3. The value of $\mathrm{Re_k}$ corresponding to the particular time during each run is shown in the legend. As $\mathrm{Re_k}$ increases incrementally, transition moves forward, as expected. From $\mathrm{Re_k} = 322$ to 554, transition moves quickly across the measurement range. At $\mathrm{Re_k} = 322$, the RMS pressure is near that for a laminar smooth-wall boundary layer. As $\mathrm{Re_k}$ is increased only slightly to 339, the RMS begins to increase at the downstream end of the experimental apparatus. For $\mathrm{Re_k} = 355$, the location where the RMS departs from laminar levels moves farther upstream. The initial increase in RMS is rapid with respect to distance. As $\mathrm{Re_k}$ increases further, the RMS follows a similar trend as transition moves forward. Again, the initial increase in RMS appears to be large. At some distance farther downstream, the RMS "overshoots" the smooth-wall turbulent value during the transition process, as is typical.[41] After the overshoot, the RMS then decreases to a value near that for a smooth-wall turbulent boundary layer. The far-downstream RMS values in Figure 9(a), however, are slightly above the smooth-wall turbulent values. This could presumably be due to residual high-energy structures within the turbulent boundary layer downstream of the roughness.

An array of pressure sensors at $x/D = 143.5$ in the pipe insert was used to record the spanwise distribution of the RMS at that location (Figure 9(b)). The sensors were located at $z/D = 0.0$, 1.8, 3.5, 5.3, 7.1, and 10.6, where z/D is the spanwise coordinate from the roughness wake centerline. Additional sensors were present at $z/D = -5.3$ and $z/D = -10.6$, and the RMS values from those sensors are plotted as solid symbols in the figure. The results indicated good symmetry of the wake. Spectra indicating the wake symmetry appear later, in Figures 15, 16, and 17. When examining the spanwise RMS, it is important to note that the state of the boundary layer is likely changing from laminar to turbulent as $\mathrm{Re_k}$ is increased. For the lowest value of $\mathrm{Re_k}$ (322), the spanwise RMS is near laminar levels. At $\mathrm{Re_k} = 339$, the RMS is highest along the wake centerline and decreases to laminar levels off the centerline. This indicates that even as far downstream as $x/D = 143.5$, the spanwise extent of the wake is relatively small. As $\mathrm{Re_k}$ increases only slightly further to 355, the spanwise extent of the wake rapidly increases to approximately 10 diameters away from the wake centerline. At this condition, the maximum RMS still occurs along the wake centerline. However, because the sensors are spaced relatively far apart, there is insufficient resolution to fully determine the maximum RMS. As $\mathrm{Re_k}$ is increased further, the maximum RMS appears to occur off the centerline of the wake, and the location of the maximum moves farther from the wake centerline. For these cases, the RMS is at or near laminar levels by $z/D = 10.6$. The maximum observed RMS occurs at $z/D = 5.3$ for $\mathrm{Re_k} = 554$.

B. Streamwise Spectra

Figures 10, 11, and 12 show power spectra along the roughness wake centerline, corresponding to the RMS data in Figure 9(a). Each figure shows three sets of spectra corresponding to a particular roughness height

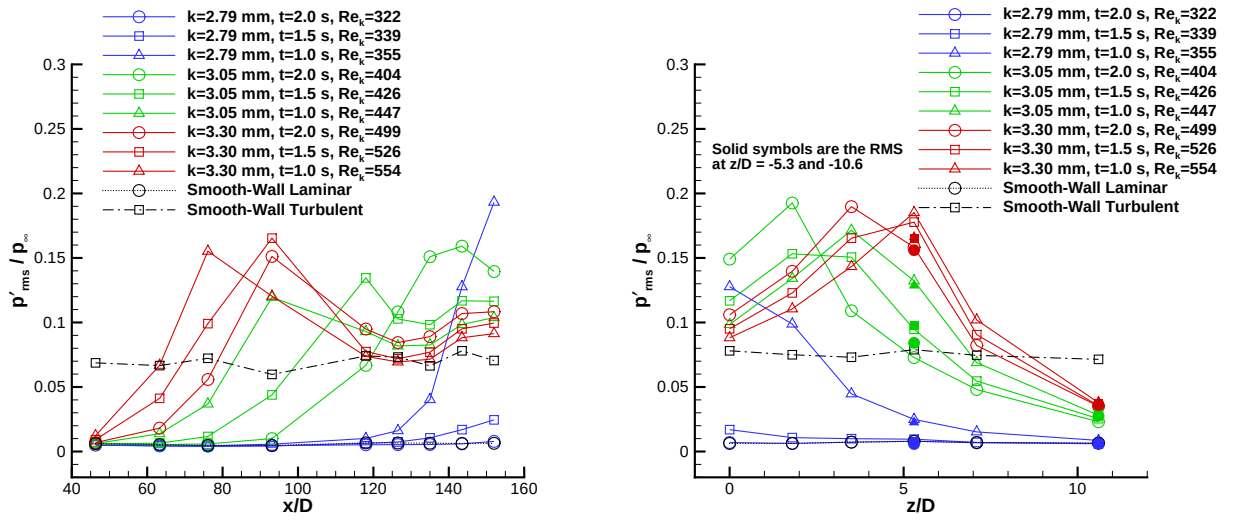

(a) Streamwise along the wake centerline

(b) Spanwise at $x/D = 143.5$

Figure 9. Effect of small changes in $\mathrm{Re_k}$ on the RMS pressure.

and a different time during each run. Figure 10 shows the spectra for $k = 2.79$ mm, Figure 11 shows the spectra for $k = 3.05$ mm, and Figure 12 shows the spectra for $k = 3.30$ mm. As $\mathrm{Re_k}$ increases, these plots show peaks developing in the spectra (presumably from instabilities within the wake). The increase in the spectral amplitudes occurs farther upstream as $\mathrm{Re_k}$ increases, and the broadening of the peaks in the spectra indicates turbulent flow. Any of these peaks could be different modes of instabilities, but stability computations are needed to identify their role in the transition process.

The spectra are again plotted in Figures 13 and 14, but organized instead by sensor location. Each figure then shows the spectra at each sensor location for all $\mathrm{Re_k}$ conditions. Figure 13 shows spectra for all values of $\mathrm{Re_k}$ along the wake centerline at $x/D = 46.3$, 63.3, 76.1, and 93.1. Figure 14 shows spectra for all values of $\mathrm{Re_k}$ along the wake centerline at $x/D = 118.0$, 135.0, 143.5, and 152.0.

At $\mathrm{Re_k} = 322$ (Figure 10(a)), the majority of the spectra along the wake centerline are nearly identical to the smooth-wall laminar spectrum. It is not until $x/D = 135.0$ and $x/D = 152.0$ that a small peak appears in the spectrum, with a frequency near 10–25 kHz. Recall that for this value of $\mathrm{Re_k}$, the RMS pressure at the downstream end of the apparatus was near laminar levels, so these peaks have small amplitudes. This peak grows in amplitude and occurs farther upstream for $\mathrm{Re_k}$ of 339 and 355 (Figures 10(b) and 10(c)). The peak appears to occur at the same frequency within the wake. For $\mathrm{Re_k} = 355$, the spectrum at $x/D = 152.0$ has amplitudes well above those of a smooth-wall turbulent spectrum, but the peak is still visible.

As $\mathrm{Re_k}$ is increased further (Figure 11), transition continues to move farther upstream but a new higher-frequency peak appears at 45–55 kHz. This higher-frequency peak is first seen for $\mathrm{Re_k} = 404$ (Figure 11(a)) at $x/D = 93.1$. For $\mathrm{Re_k} = 426$ and higher, the lower-frequency peak at 15–35 kHz begins to resemble a "double peak", a main peak with two narrow maxima. The streamwise location at which the higher-frequency peak first appears moves farther upstream for $\mathrm{Re_k} = 426$ and 447 (Figures 11(b) and 11(c)). Unlike the lower-frequency peak, the higher-frequency peak seems to decrease in frequency with downstream distance.

The same trends are seen for $\mathrm{Re_k} = 499$ through 554 (Figure 12). However, the changes in the spectra are less drastic for these higher Reynolds numbers, compared to the changes in the spectra observed about the near-critical Reynolds number, $\mathrm{Re_k} = 355$. Again, this is likely due to the increased sensitivity of transition for conditions near those for critical roughness.

C. Spanwise Spectra

Figures 15, 16, and 17 show the spanwise spectra for the data appearing in Figure 9(b). These spanwise spectra were computed from the array of sensors at $x/D = 143.5$ within the pipe insert. Since this location is significantly downstream from the roughness, the flow is likely turbulent for most of the values of $\mathrm{Re_k}$ shown here. In the figures, results from $z/D = 5.3$ and $z/D = -5.3$, as well as $z/D = 10.6$ and $z/D = -10.6$,

are shown to agree well, demonstrating the symmetry of the wake. When analyzing the results here, it is important to consider the possibility that the flow is turbulent for some conditions when comparing to computations of instabilities that assume laminar flow.

At the lowest value of $\mathrm{Re_k} = 322$ (Figure 15(a)), the peak at 10–25 kHz that occurred on the centerline in Figure 10(a) appears to be strongest along the centerline of the wake. It has the highest amplitude at $z/D = 0.0$ and the amplitude decreases with increasing spanwise distance. Two peaks at 13 and 36 kHz appear off the centerline of the wake and are not seen along the centerline. The peak at 36 kHz appears strongest at $z/D = 5.3$.

At a slightly higher $\mathrm{Re_k}$ of 339 (Figure 15(b)), the amplitudes of peaks in the spectra increase, though the amplitudes at $z/D = 10.3$ are not noticeably higher than for $\mathrm{Re_k} = 322$. The strongest peak is again on the wake centerline near 10–25 kHz. A large change in the spectra becomes evident at $\mathrm{Re_k} = 355$ (Figure 15(c)). At this condition, the spectra along the centerline appear turbulent. Throughout the wake, there is a single large peak centered around a frequency of 25 kHz. The peak decreases in amplitude away from the wake centerline, but the peak frequency remains the same.

As $\mathrm{Re_k}$ increases from 404–554 (Figures 16 and 17), the trends in the spectra are similar. Spectra along the wake centerline indicate that the flow is becoming turbulent there with increasing $\mathrm{Re_k}$. In addition, the maximum amplitudes of the spectra occur farther off the wake centerline as $\mathrm{Re_k}$ is increased. Away from the centerline, a single large peak is seen as the spectra decrease towards laminar levels. At these higher values of $\mathrm{Re_k}$, the wake still has significant fluctuations as far off the centerline as $z/D = 10.6$.

VI. Summary

Transition due to roughness on the surface of a reentry vehicle can cause high levels of skin friction and heating in flight. Currently, empirical correlations are used by designers to predict the onset of transition, however these correlations can contain large uncertainty. Future generations of prediction methods could be based upon the physical mechanisms responsible for roughness-induced transition, which are at present poorly understood. In order to develop physics-based prediction methods, a greater understanding of these instability mechanisms is required. In the present work, controlled experimental measurements of disturbances were made in the wake of an isolated cylindrical roughness element within the laminar nozzle-wall boundary layer of the Boeing/AFOSR Mach-6 Quiet Tunnel at Purdue University.

Disturbances that are likely due to instabilities leading to incipient transition from near-critical isolated roughness elements were reported in this paper. Pressure sensors were installed on the tunnel centerplane at $x/D = 46.3$, 63.3, 76.1, 93.1, 118.0, 126.5, 135.0, 143.5, and 152.0. Additional sensors were installed in a spanwise array at $x/D = 143.5$. Approximately 100 runs were performed with an initial stagnation pressure of 95 psia, using a variety of roughness heights. Data were first analyzed at a time of 1.0 s into the run so that data could be compared at a similar freestream Reynolds number.

The RMS surface pressure, power spectra, and time traces were analyzed to determine instability and transition along the roughness wake centerline. At this particular tunnel condition, a roughness height near 2.79 mm ($\mathrm{Re_k} = 355$) was found to cause incipient transition at the far downstream end of the apparatus. Below this height, the boundary layer remained laminar. Above this height, transition moved forward towards the roughness as the height of the roughness was increased. A variety of peaks were detected in the spectra. These peaks are likely instabilities developing within the roughness wake that lead to transition. When repeated runs were examined, it was found that small changes in the experimental parameters may have a large effect on the transition process for the near-critical height of 2.79 mm. The transition location was observed to vary greatly during repeated runs at this height with nominally similar experimental conditions. The main uncertainty could be the varying nozzle temperatures between runs, which could alter the boundary-layer thickness relative to the roughness height. At roughness heights of 3.05 mm and 3.30 mm, the repeated runs showed more similar results. It is possible that these larger heights are less critical and transition is less sensitive to the slight variations in experimental conditions.

The overall transition process for these near-critical roughness heights appeared to occur in a similar manner for all cases. Initial growth appeared concentrated in a lower-frequency set of peaks that occurred within the 20–40 kHz frequency range for runs at $p_{0,i} = 95$ psia. These peaks grew in amplitude with downstream distance but did not appear to change frequency as they did so. A higher-frequency peak typically appeared at some location downstream of the initial growth of the lower-frequency peak. This higher-frequency peak typically occurred in the 40–70 kHz frequency range for runs at $p_{0,i} = 95$ psia.

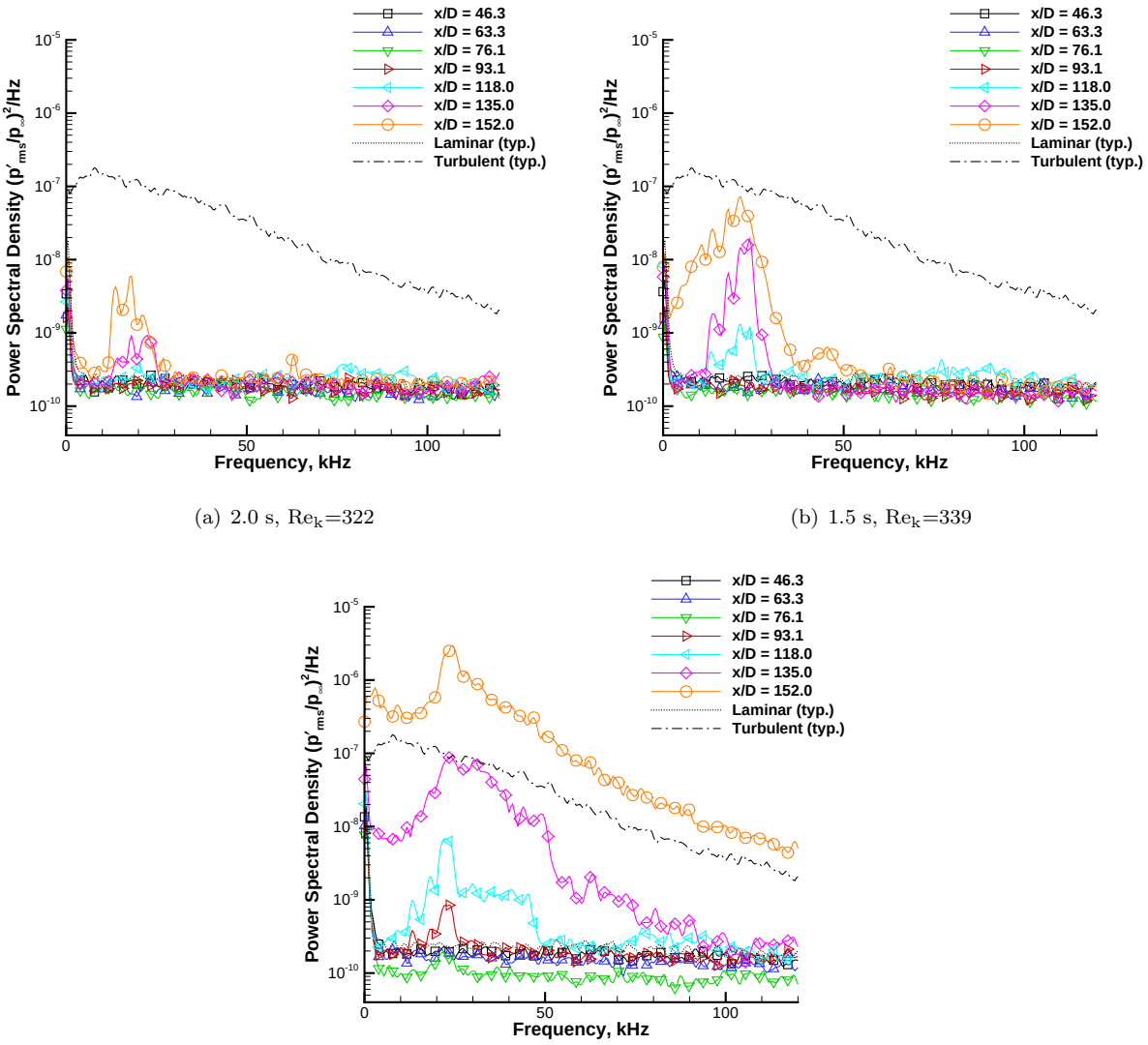

(a) 2.0 s, $\mathrm{Re_k}$=322

(b) 1.5 s, $\mathrm{Re_k}$=339

(c) 1.0 s, $\mathrm{Re_k}$=355

Figure 10. Effect of small changes in $\mathrm{Re_k}$ on the spectra along the wake centerline ($k = 2.79$ mm).

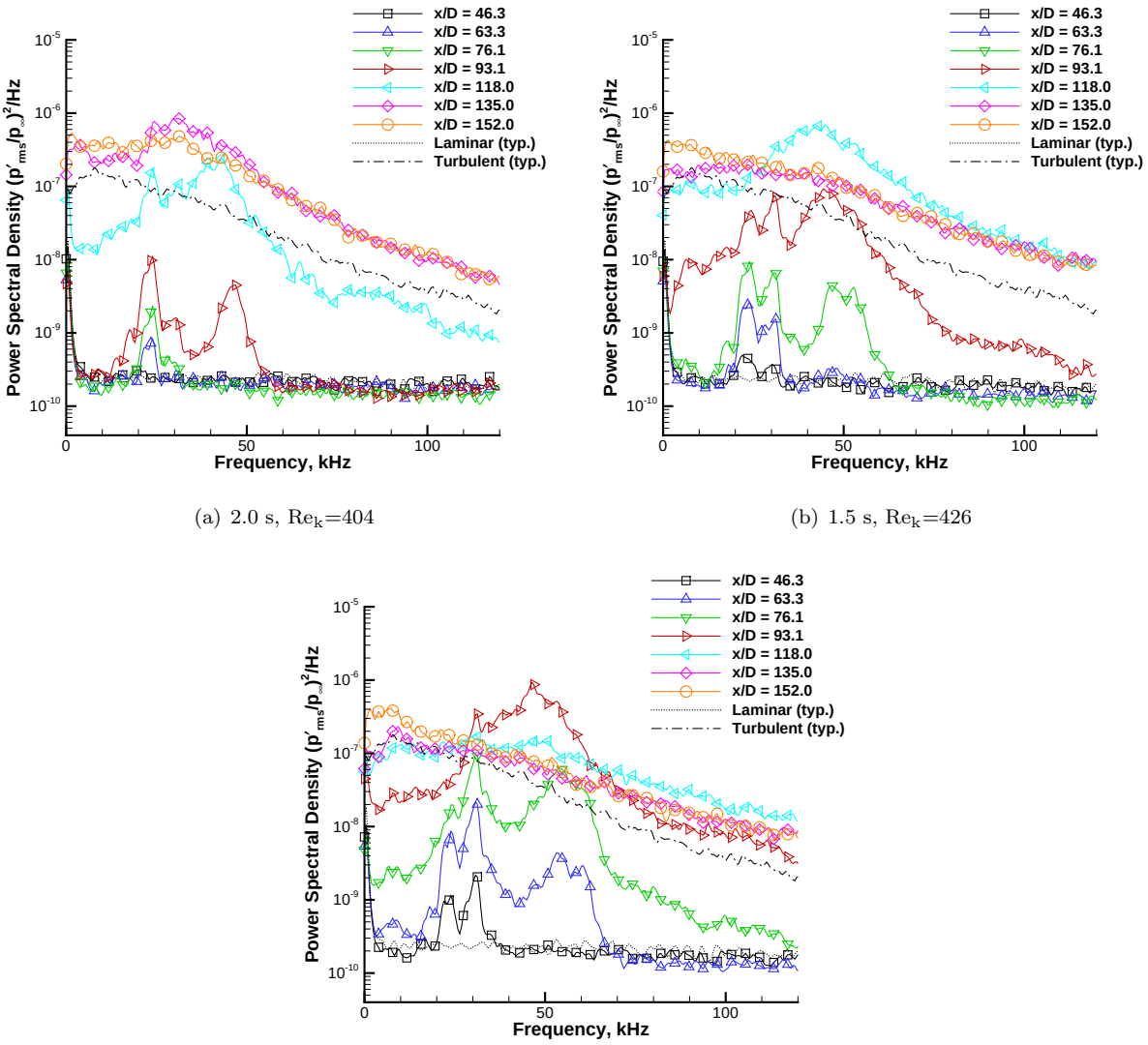

(a) 2.0 s, $\mathrm{Re_k}$=404

(b) 1.5 s, $\mathrm{Re_k}$=426

(c) 1.0 s, $\mathrm{Re_k}$=447

Figure 11. Effect of small changes in $\mathrm{Re_k}$ on the spectra along the wake centerline ($k = 3.05$ mm).

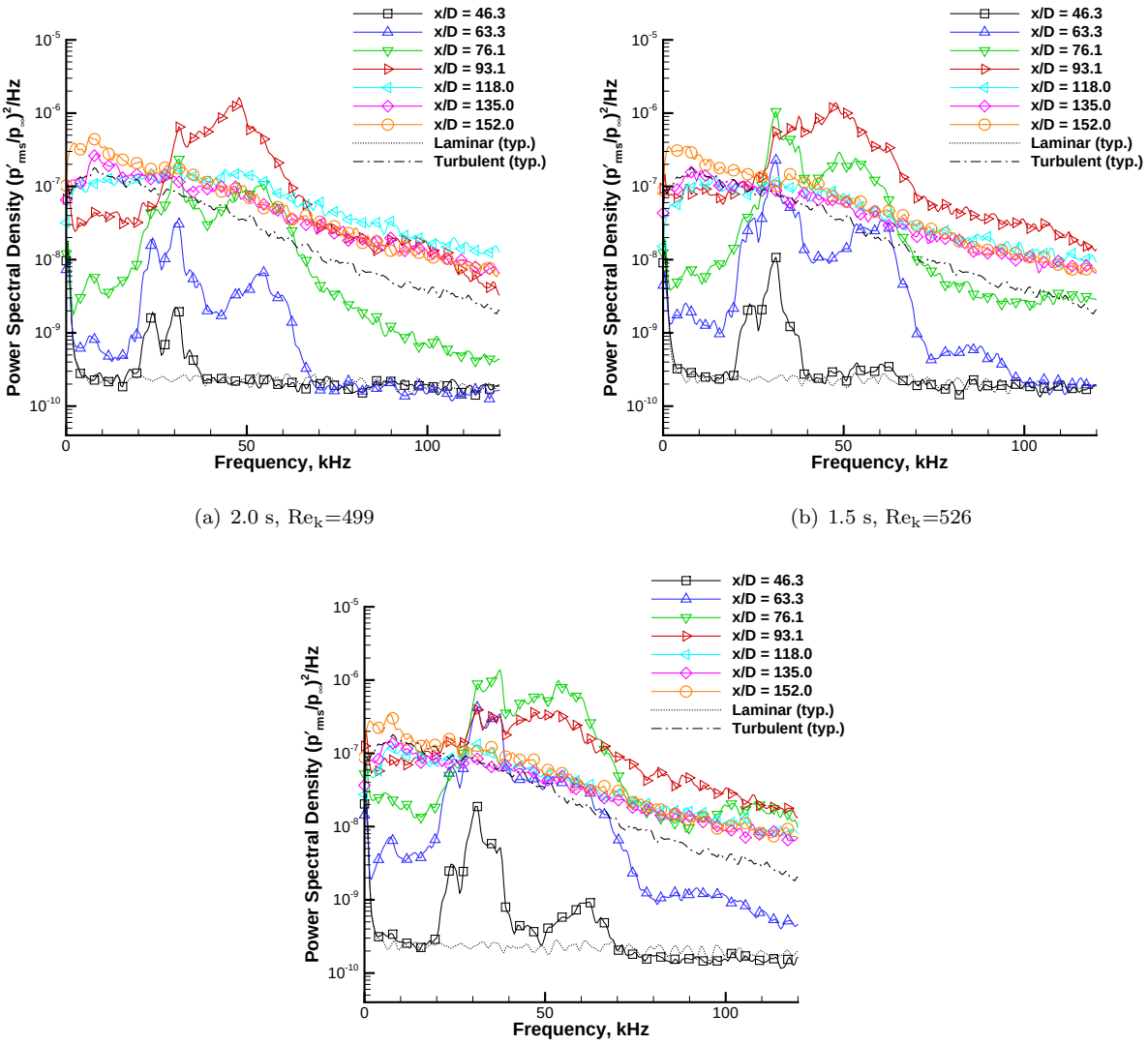

(a) 2.0 s, $\mathrm{Re_k}$=499

(b) 1.5 s, $\mathrm{Re_k}$=526

(c) 1.0 s, $\mathrm{Re_k}$=554

Figure 12. Effect of small changes in $\mathrm{Re_k}$ on the spectra along the wake centerline ($k = 3.30$ mm).

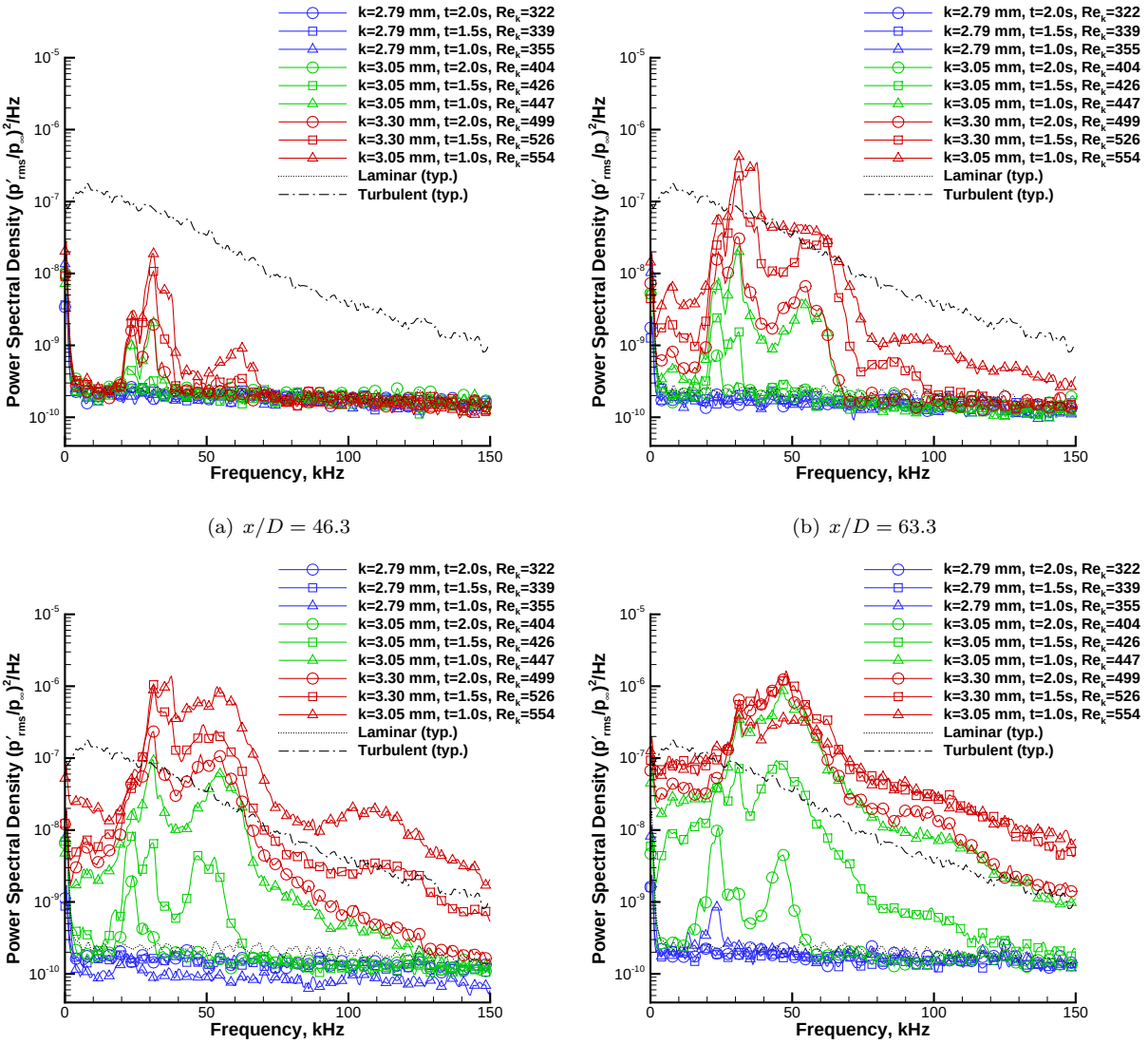

(a) $x/D = 46.3$

(b) $x/D = 63.3$

(c) $x/D = 76.1$

(d) $x/D = 93.1$

Figure 13. Effect of small changes in $\mathrm{Re_k}$ on the spectra along the wake centerline ($x/D = 46.3$, 63.3, 76.1, and 93.1).

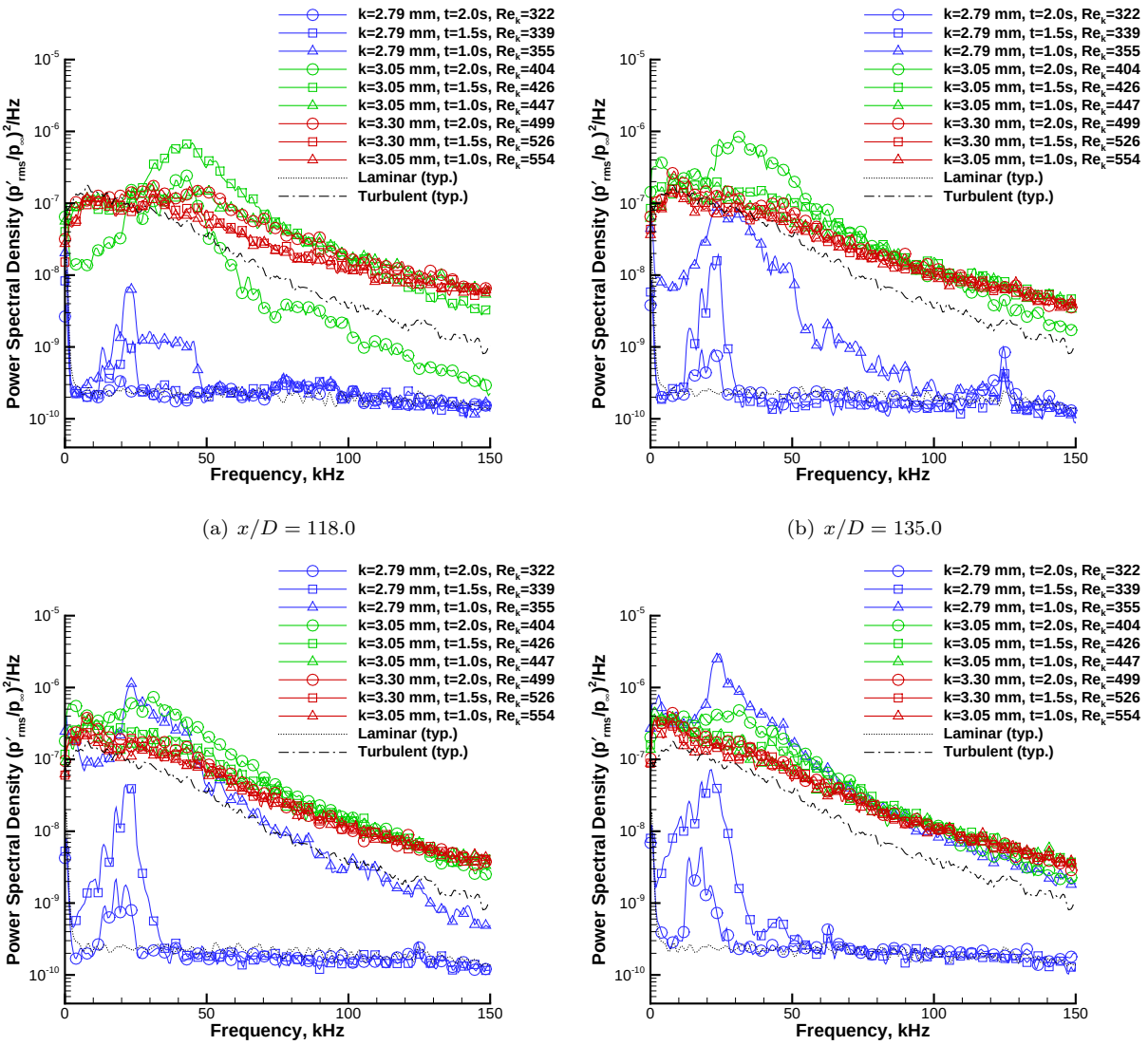

(a) $x/D = 118.0$

(b) $x/D = 135.0$

(c) $x/D = 143.5$

(d) $x/D = 152.0$

Figure 14. Effect of small changes in $\mathrm{Re_k}$ on the spectra along the wake centerline ($x/D = 118.0$, 135.0, 143.5, and 152.0).

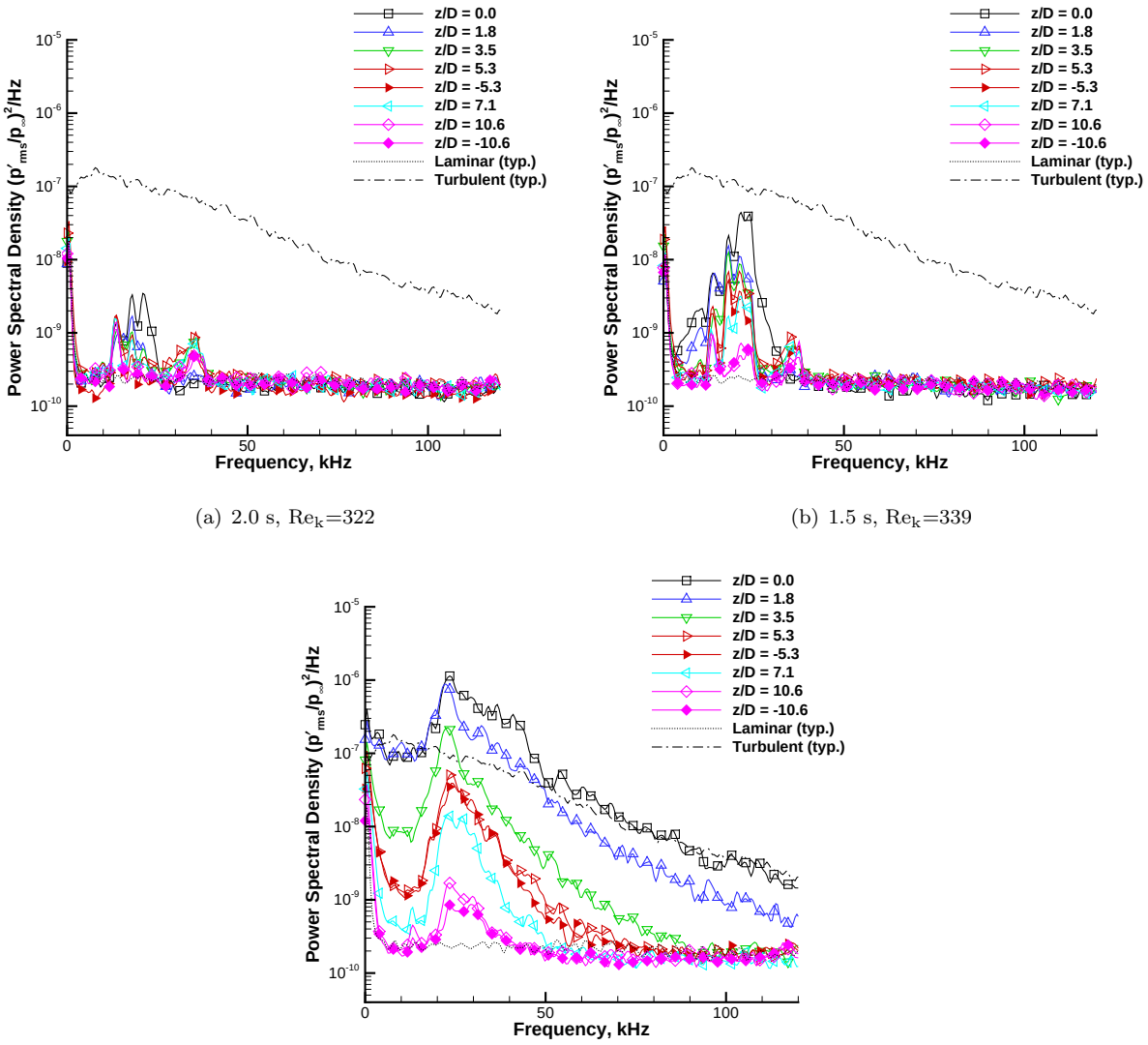

(a) 2.0 s, $\mathrm{Re_k}$=322

(b) 1.5 s, $\mathrm{Re_k}$=339

(c) 1.0 s, $\mathrm{Re_k}$=355

Figure 15. Effect of small changes in $\mathrm{Re_k}$ on the spanwise spectra at $x/D = 143.5$ ($k = 2.79$ mm).

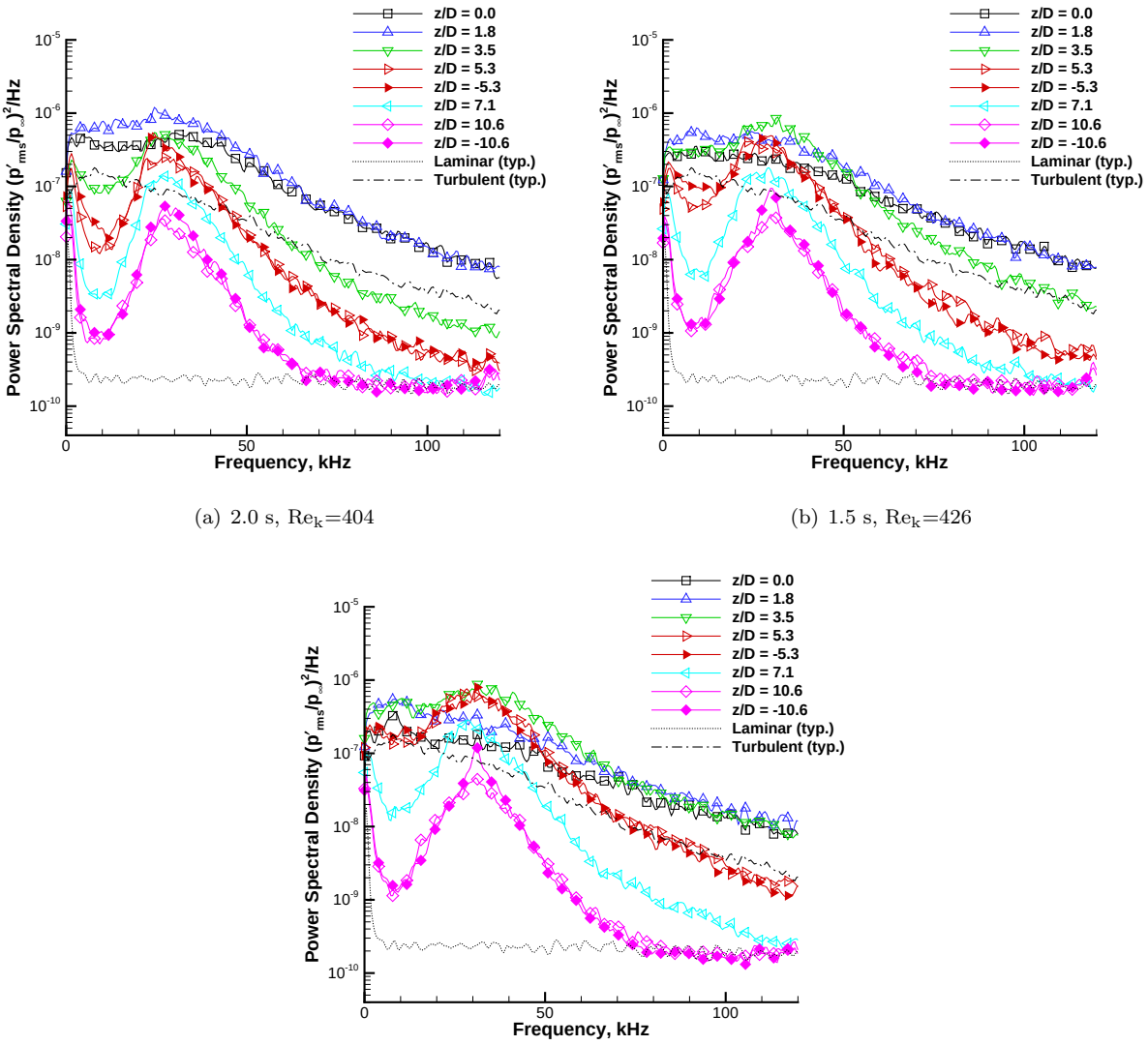

(a) 2.0 s, $\mathrm{Re_k}$=404

(b) 1.5 s, $\mathrm{Re_k}$=426

(c) 1.0 s, $\mathrm{Re_k}$=447

Figure 16. Effect of small changes in $\mathrm{Re_k}$ on the spanwise spectra at $x/D = 143.5$ ($k = 3.05$ mm).

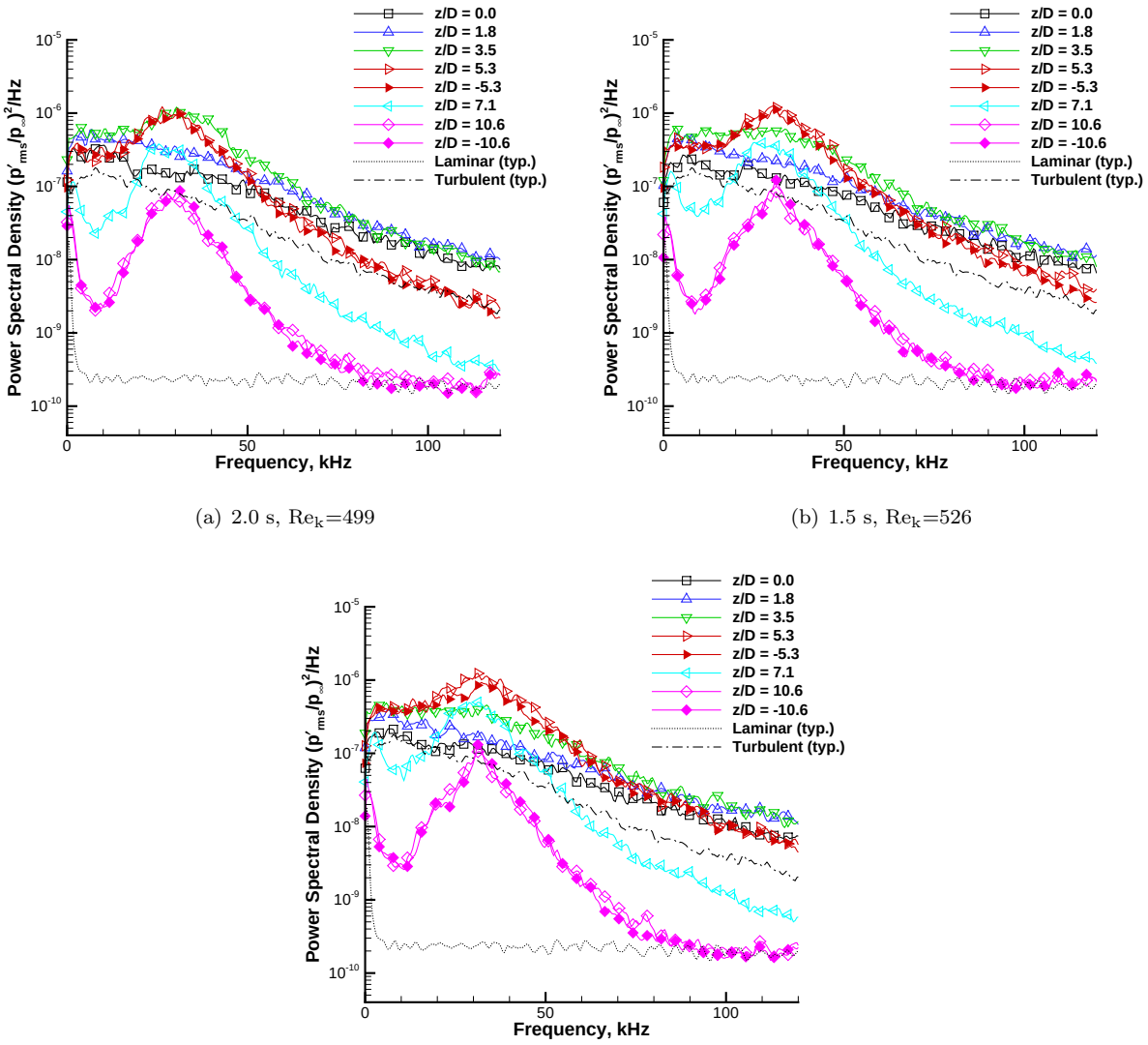

(a) 2.0 s, $\mathrm{Re_k}$=499

(b) 1.5 s, $\mathrm{Re_k}$=526

(c) 1.0 s, $\mathrm{Re_k}$=554

Figure 17. Effect of small changes in $\mathrm{Re_k}$ on the spanwise spectra at $x/D = 143.5$ ($k = 3.30$ mm).

The higher-frequency peak was possibly related to the boundary-layer thickness, as its frequency seemed to decrease slightly with downstream distance. As the flow began to transition, the peaks appeared to broaden and merge as the fluctuation amplitudes approached and overshot the smooth-wall turbulent values. Eventually, the fluctuation amplitudes decreased towards the smooth-wall turbulent values and the peaks broadened, suggesting turbulent flow. Spectra from the spanwise sensors off the wake centerline suggested that transition occurred first along the centerline. The region of disturbed flow then appeared to spread outward in the spanwise direction as $\mathrm{Re_k}$ increased. The transition process appeared to move quickly across the experimental measurement range when $\mathrm{Re_k}$ varied from 322–554, but across this range the spectra qualitatively indicated that the disturbances grew in a similar manner.

It is not possible to describe the physics of transition for these near-critical roughnesses based solely on these experimental measurements. The experimental measurements were able to identify disturbance frequencies and amplitudes from the real fluid physics involved in the transition process, but only at certain locations. To fully understand the mechanisms of transition for these cases, separate stability computations are needed to compare to these results.

Acknowledgments

This research was funded by the NASA Fundamental Aeronautics Hypersonics Program (grant 102361), the NASA Constellation University Institutes Program (award Z634003), and the Air Force Office of Scientific Research (grant FA9550-09-1-0191). The majority of the hardware used in these experiments was fabricated by the skilled machinists in the Purdue AAE department machine shop.

References

[1]Reshotko, E., "Transition Issues for Atmospheric Entry," *Journal of Spacecraft and Rockets*, Vol. 45, No. 2, March-April 2008, pp. 161–164.

[2]Schneider, S. P., "Effects of Roughness on Hypersonic Boundary-Layer Transition," *Journal of Spacecraft and Rockets*, Vol. 45, No. 2, March-April 2008, pp. 193–209.

[3]Smith, A. M. O. and Gamberoni, N., "Transition, Pressure Gradient and Stability Theory," Douglas Aircraft Company Report No. ES 26388, August 1956.

[4]van Ingen, J., "The e^N method for transition prediction. Historical review of work at TU Delft," AIAA Paper 2008-3830, June 2008.

[5]Reed, H. L., Saric, W. S., and Arnal, D., "Linear Stability Theory Applied to Boundary Layers," *Annual Review of Fluid Mechanics*, Vol. 28, 1996, pp. 389–428.

[6]Malik, M. R., "Hypersonic Flight Transition Data Analysis Using Parabolized Stability Equations with Chemistry Effects," *Journal of Spacecraft and Rockets*, Vol. 40, No. 3, May-June 2003, pp. 332–344.

[7]Whitehead, A. H., "Flow Field and Drag Characteristics of Several Boundary-Layer Tripping Elements in Hypersonic Flow," Tech. Rep. TN D-5454, NASA Langley Research Center, October 1969.

[8]Liepmann, H. W. and Fila, G. H., "Investigations of Effects of Surface Temperature and Single Roughness Elements on Boundary-Layer Transition," NACA Report 890, 1947.

[9]Klebanoff, P. S. and Tidstrom, K. D., "Mechanism by Which a Two-Dimensional Roughness Element Induces Boundary-Layer Transition," *The Physics of Fluids*, Vol. 15, No. 7, July 1972, pp. 1173–1188.

[10]Klebanoff, P. S., Cleveland, W. G., and Tidstrom, K. D., "On the Evolution of a Turbulent Boundary Layer Induced by a Three-Dimensional Roughness Element," *Journal of Fluid Mechanics*, Vol. 237, 1992, pp. 101–187.

[11]Chang, C.-L. and Choudhari, M. M., "Hypersonic Viscous Flow over Large Roughness Elements," AIAA Paper 2009-0173, January 2009.

[12]Greene, P. T., Eldredge, J. D., Zhong, X., and Kim, J., "A Numerical Study of Purdue's Mach 6 Tunnel with a Roughness Element," AIAA Paper 2009-174, January 2009.

[13]Choudhari, M., Li, F., Wu, M., Chang, C.-L., and Edwards, J., "Laminar-Turbulent Transition behind Discrete Roughness Elements in a High-Speed Boundary Layer," AIAA Paper 2010-1575, January 2010.

[14]Chang, C.-L., Choudhari, M. M., and Li, F., "Numerical Computations of Hypersonic Boundary-Layer over Surface Irregularities," AIAA Paper 2010-1572, January 2010.

[15]Bartkowicz, M. D., Subbareddy, P. K., and Candler, G. V., "Numerical Simulations of Roughness Induced Instability in the Purdue Mach 6 Wind Tunnel," AIAA Paper 2010-4723, June 2010.

[16]Iyer, P. S., Muppidi, S., and Mahesh, K., "Transition of Hypersonic Flow past Flat Plate with Roughness Elements," AIAA Paper 2010-5015, June 2010.

[17]Yoon, S., Barnhardt, M. D., and Candler, G. V., "Simulations of High-Speed Flow over an Isolated Roughness," AIAA Paper 2010-1573, January 2010.

[18]Iyer, P. S., Muppidi, S., and Mahesh, K., "Roughness-Induced Transition in High Speed Flows," AIAA Paper 2011-566, January 2011.

[19]Marxen, O., Iaccarino, G., and Shaqfeh, E. S. G., "Numerical Simulations of Hypersonic Boundary-Layer Instability with Localized Roughness," AIAA 2011-567, January 2011.

[20]Chang, C.-L., Choudhari, M. M., and Li, F., "Effects of Cavities and Protuberances on Transition over Hypersonic Vehicles," AIAA Paper 2011-3245, June 2011.

[21]Greene, P. T., Eldredge, J. D., Zhong, X., and Kim, J., "Numerical Study of Hypersonic Flow Over an Isolated Roughness with a High-Order Cut-Cell Method," AIAA Paper 2011-3249, June 2011.

[22]Wheaton, B. M., Bartkowicz, M. D., Subbareddy, P. K., Schneider, S. P., and Candler, G. V., "Roughness-Induced Instabilities at Mach 6: A Combined Experimental and Numerical Study," AIAA Paper 2011-3248, June 2011.

[23]Iyer, P. S., Muppidi, S., and Mahesh, K., "Boundary Layer Transition in High-Speed Flows due to Roughness," AIAA Paper 2012-1106, January 2012.

[24]Bernardini, M., Pirozzoli, S., and Orlandi, P., "Compressibility Effects on Roughness-Induced Boundary Layer Transition," *International Journal of Heat and Fluid Flow*, Vol. 35, June 2012, pp. 45–51.

[25]Kegerise, M. A., Owens, L. R., and King, R. A., "High-Speed Boundary-Layer Transition Induced by an Isolated Roughness Element," AIAA Paper 2010-4999, June 2010.

[26]Kegerise, M., King, R., Owens, L., Choudhari, M., Norris, A., Li, F., and Chang, C.-L., "An Experimental and Numerical Study of Roughness-Induced Instabilities in a Mach 3.5 Boundary Layer," In proceedings of NATO RTO-MP-AVT-200, San Diego, CA, May 2012.

[27]Ergin, F. G. and White, E. B., "Unsteady and Transitional Flows Behind Roughness Elements," *AIAA Journal*, Vol. 44, No. 11, November 2006, pp. 2504–2514.

[28]Rizzetta, D. P. and Visbal, M. R., "Direct Numerical Simulations of Flow Past an Array of Distributed Roughness Elements," *AIAA Journal*, Vol. 45, No. 8, August 2007, pp. 1967–1976.

[29]Wheaton, B. M. and Schneider, S. P., "Roughness-Induced Instability in a Hypersonic Laminar Boundary Layer," *AIAA Journal*, Vol. 50, No. 6, June 2012, pp. 1245–1256.

[30]Wheaton, B. M., *Roughness-Induced Instabilities in a Mach-6 Laminar Boundary Layer*, Ph.D. thesis, Purdue University School of Aeronautics & Astronautics, West Lafayette, IN, December 2012.

[31]Bartkowicz, M. D., *Numerical Simulations of Hypersonic Boundary Layer Transition*, Ph.D. thesis, University of Minnesota, Minneapolis, MN, January 2012.

[32]Schneider, S. P., "Development of Hypersonic Quiet Tunnels," *Journal of Spacecraft and Rockets*, Vol. 45, No. 4, July-August 2008, pp. 641–664.

[33]Juliano, T. J., Schneider, S. P., Aradag, S., and Knight, D., "Quiet-Flow Ludwieg Tube for Hypersonic Transition Research," *AIAA Journal*, Vol. 46, No. 7, July 2008, pp. 1757–1763.

[34]Casper, K. M., Beresh, S. J., and Schneider, S. P., "Pressure Fluctuations Beneath Turbulent Spots and Instability Wave Packets in a Hypersonic Boundary Layer," AIAA Paper 2011-372, January 2011.

[35]Estorf, M., Radespiel, R., Schneider, S. P., and Johnson, H. B., "Surface-Pressure Measurements of Second-Mode Instability in Quiet Hypersonic Flow," AIAA Paper 2008-1153, January 2008.

[36]Harris, J. E. and Blanchard, D. K., "Computer Program for Solving Laminar, Transitional, or Turbulent Compressible Boundary-Layer Equations for Two-Dimensional and Axisymmetric Flow," NASA Technical Report TM-83207, February 1982.

[37]Skoch, C. R., *Final Assembly and Initial Testing of the Purdue Mach-6 Quiet-Flow Ludwieg Tube*, Master's thesis, Purdue University School of Aeronautics & Astronautics, West Lafayette, IN, August 2001.

[38]Schneider, S. P., Rufer, S. J., Randall, L., and Skoch, C. R., "Shakedown of the Purdue Mach-6 Quiet-Flow Ludwieg Tube," AIAA Paper 2001-0457, January 2001.

[39]Sivells, J. C., "A Computer Program for the Aerodynamic Design of Axisymmetric and Planar Nozzles for Supersonic and Hypersonic Wind Tunnels," Technical Report AEDC-TR-78-63, Arnold Engineering Development Center, December 1978.

[40]Steen, L. E., *Characterization and Development of Nozzles for a Hypersonic Wind Tunnel*, Master's thesis, Purdue University School of Aeronautics & Astronautics, West Lafayette, IN, December 2010.

[41]Martellucci, A., Chaump, L., and Rogers, D., "Experimental Determination of the Aeroacoustic Environment about a Slender Cone," *AIAA Journal*, Vol. 11, No. 5, May 1973, pp. 634–642.

[42]Smith, A. M. O. and Clutter, D. W., "The Smallest Height of Roughness Capable of Affecting Boundary-Layer Transition," *Journal of the Aerospace Sciences*, Vol. 26, April 1959, pp. 229–245.

[43]Van Driest, E. R. and McCauley, W. D., "The Effect of Controlled Three-Dimensional Roughness on Boundary-Layer Transition at Supersonic Speeds," *Journal of the Aerospace Sciences*, Vol. 27, No. 4, April 1960, pp. 261–271,303.

[44]Van Driest, E. R. and Blumer, C. B., "Boundary-Layer Transition at Supersonic Speeds – Three-Dimensional Roughness Effects (Spheres)," *Journal of the Aerospace Sciences*, Vol. 29, August 1962, pp. 909–916.

[45]Holloway, P. F. and Sterrett, J. R., "Effect of Controlled Surface Roughness on Boundary Layer Transition and Heat Transfer at Mach Numbers of 4.8 and 6.0," NASA TN-D-2054, April 1964.

[46]Reda, D. C., Wilder, M. C., and Prabhu, D. K., "Transition Experiments on Blunt Bodies with Isolated Roughness Elements in Hypersonic Free Flight," AIAA Paper 2010-1367, January 2010.

[47]Casper, K. M., Johnson, H. B., and Schneider, S. P., "Effect of Freestream Noise on Roughness-Induced Transition for a Slender Cone," *Journal of Spacecraft and Rockets*, Vol. 48, No. 3, May-June 2011, pp. 406–413.

[48]Chou, A., Wheaton, B. M., Ward, C. A. C., Gilbert, P. L., Steen, L. E., and Schneider, S. P., "Instability and Transition Research in a Mach-6 Quiet Tunnel," AIAA Paper 2011-283, January 2011.